Computational Description of Key Spectroscopic Features of Zeolite SSZ-13

Florian Göltl[1,2,], Alyssa M Love[1], Sarah C. Schuenzel[2], Patrick Wolf[1], Manos Mavrikakis[2,*], Ive Hermans[1,2,*]*

[1] Department of Chemistry, University of Wisconsin – Madison, 53706 Madison, WI, USA

[2] Department of Chemical and Biological Engineering, University of Wisconsin – Madison, 53706 Madison, WI, USA

e-Mail: fgoeltl@wisc.edu, emavrikakis@wisc.edu, hermans@chem.wisc.edu

Abstract

The catalytic properties of zeolites are intimately linked to the distribution of Al atoms and defects in the pore network and their relative positions. However, characterizing this distribution is challenging, in particular when different local Al arrangements are considered. In this contribution we use a combination of first principles calculations and experimental measurements to develop a model for the Al-distribution in protonated SSZ-13. We furthermore apply this model to understand trends in OH-IR, ^{27}Al-NMR and ^{29}Si-NMR spectra. We use a Boltzmann distribution to predict the proton position for a given local Al configuration and show that for each configuration several H positions are occupied. Therefore a multi-peak spectrum in OH-IR vibrational spectroscopy is observed for all Al configurations, which is in line with experimentally measured spectra for zeolites at different Si/Al ratios. From NMR spectroscopy we find that the proton position leads to significant shifts in ^{27}Al-NMR and ^{29}Si-NMR spectra due to the modification of the local strain, which is lost when a uniform background charge is introduced. These findings are supported by experimental measurements. Finally we discuss the

shortcomings of the presented model in terms of unit cell size and the impact of adjacent unit cells.

Introduction:

Zeolites are a class of crystalline materials where corner sharing SiO_4 tetrahedra form a complex network of cavities and channels. In their purely siliceous form they are chemically inert, but they can be functionalized by substituting Si atoms by Al atoms. This substitution leads to a localized charge deficiency, which in turn is compensated for by the presence of a cation. This cation can serve as active site for adsorption or catalytic conversion. However, the macroscopic performance of zeolites does not only depend on their chemical composition, but also on the exact location of the Al atoms within the pore network. Adsorbed molecules will experience differences in confinement effects due to their location within the pore network[1–4], local strain at the active centers can alter the chemical activity of the active centers[5–8] and the relative positioning of anchoring points with respect to each other can lead to different active site motifs[9,10].

Up until today only very few rules for Al distribution, such as the Loewenstein rule (i.e. Al atoms will not occupy neighboring T-sites) have been established[11]. At the same time characterizing the distribution of Al atoms in zeolites proves to be challenging due to the similarity between Si and Al. Alberti et al. used XRD measurements to identify the average T-O distance in Mordenite[12]. Since the T-O bond is elongated for T=Al compared to T=Si, they were able to deduce information about the T-site occupancy in the zeolite. Furthermore Sastre et al. used a

combination of experimental measurements and computations for OH-IR vibrational frequencies to establish a correlation between Al-distribution and synthesis parameters for ITQ-7 zeolites[13], a concept that has recently been applied by Losch et al. to understand Al locations in ZSM-5 zeolites[14]. Similar conclusions were reached by Dedecek, Sklenak and Sauer et al., who used NMR spectroscopy to identify the Al distributions in several zeolite frameworks[15–18]. Furthermore van Bokhoven et al. used the X-ray standing wave technique to elucidate the position of Al atoms in scolecite zeolite[19].

Despite the success for specific systems, a general understanding of the Al distribution is still missing. This is mainly due to the fact that the methods outlined above lead to average occupations of T-sites with different local symmetries. This type of information is sufficient for zeolites with high Si/Al ratios, where Al atoms are assumed to be well separated. However, information on the relative position of Al atoms with respect to each other, which is important for zeolites with low to medium Si/Al ratios, cannot be obtained using these methods. This shortcoming is even more significant for transition metal exchanged zeolites, where the local configuration of Al atoms determines the active sites formed[5,9,10,20,21]. Furthermore recent work has shown that Al proximity impacts the NH_3 adsorption strength, a descriptor for chemical activity. One way to access the local proximity of Al atoms was developed by Dedecek et al.. They used the maximum Co loading in Ferrierite to determine the fraction of paired Al atoms[17], a method that was subsequently adapted by Gounder et al. to determine the amount of paired Al atoms in SSZ-13[22]. It is assumed that this method can identify Al atoms that are close enough to bind Co,

but using this method alone it is not clear which rings the Al atoms occupy or whether they are separated by one, two or three Si atoms. Additionally, this method requires the exchange of Co, which significantly modifies the properties of the parent zeolite framework and the original sample cannot be recovered for further experiments.

It would therefore be highly desirable to arrive at a more detailed understanding of the local proximity of Al atoms in zeolites. Ideally such an understanding would be based on widely available experimental methods such as OH-IR spectroscopy[13] or NMR spectroscopy and would be rooted in a fundamentally sound model for the studied zeolite catalyst. Over the past years the zeolite SSZ-13 started to play a key role as model system to understand zeolite catalysts. From an application standpoint, this increased interest originates from the efficiency of the Cu exchanged form of SSZ-13 in deNO_x-SCR[23,24] and in the conversion of methane to methanol[9,25,26]. From a fundamental point of view it is rooted in SSZ-13 being a zeolite in the chabazite structure, the zeolite framework with the smallest primitive unit cell and an ideal model system for zeolite catalysis. However, as of today no consistent and general model to describe OH-IR and NMR spectroscopies has been developed for this system.

In this contribution we develop a theoretical model for proton positions in the zeolite SSZ-13 based on DFT calculations and thermodynamic models. We study various different local Al configurations for Si/Al ratios of 5 and 11. Based on this model we then explain the experimentally observed trends in OH-IR vibrational spectra and NMR spectra in different SSZ-13 samples.

A model for H-SSZ-13

In this contribution we focus on SSZ-13, a zeolite in the chabazite framework. This framework is the zeolite framework with the smallest primitive unit cell, which contains 12 symmetrically equivalent T-sites (chemical composition $Si_{12}O_{24}$) arranged in a double six-ring structure. Most of the calculations reported in this work are performed for the primitive unit cell. If another unit cell was used, it will be explicitly mentioned in the text. The framework can be activated by substituting Si atoms with Al atoms and in the theoretical part of this work we focus on unit cells containing one (Si/Al=11) or two Al (Si/Al=5) atoms. In the literature it has been shown that Al-O-Si-O-Al configurations do not exist in pentasil zeolites[27,28]. Similar work for SSZ-13 is still missing, and we therefore consider all symmetrically different possibilities to distribute Al in the primitive unit cell of SSZ-13. Only one possible 1Al unit cell exists, but five symmetrically different unit cells for 2 Al atoms can be constructed (hereafter called Al configurations) under the assumption of the validity of the Loewenstein rule (denoted $2Al^A$ through $2Al^E$, see Fig. 1 A)[29]. Each Al atom generates a local negative charge, which will be compensated for by the presence of one proton. Here we consider all possible H positions, which leads to four possibilities when 1 Al is present in the unit cell (see Fig 1 B) and 16 possibilities for 2 Al atoms in the unit cell. Furthermore, we include a silanol defect in our analysis (see Fig. 1 C). To keep the discussion short and focused, we will therefore introduce the applied methodology in detail for the 1 Al case and provide

the data and the results for the 2 Al configurations and defect sites. In a realistic system we expect that a distribution of different local Al configurations and defect geometries is present. We therefore choose the unit cell volume as 830 $Å^3$ and restrict the unit cell shape to the shape for the purely siliceous case[30], if not explicitly stated otherwise. This choice is motivated in the supporting information section S 1. In the course of this work we furthermore focus on presenting large amounts of data in an accessible way in the main text and numerical values and structures are given in the supporting data file in the supporting information.

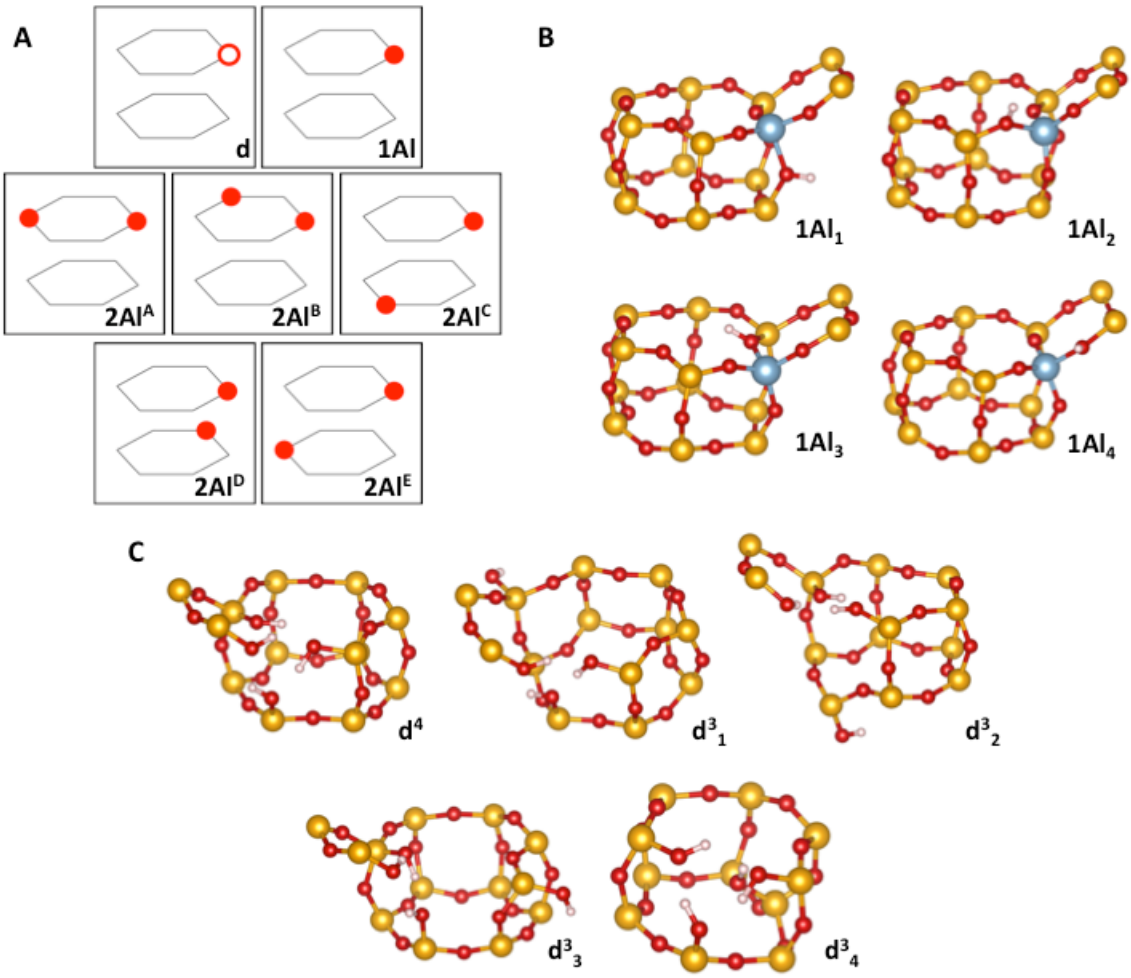

Figure 1: *A: Local Al configurations and silanol defect structures studied in this work. Black lines represent bridging oxygen bonds, a red ring the position of a silanol defect and a filled red circle the position of an Al atom. B: Four symmetrically different proton positions around an Al atom. Here the 1Al case is shown. C: Different local arrangements of silanol groups for a silanol defect. In atomistic pictures, Si is shown as yellow sphere, O as red sphere, H as white sphere and Al as grey-blue sphere.*

The 1 Al case: While all T-sites are symmetrically equivalent in SSZ-13, four symmetrically different O-atoms exist, which are shown in Fig. 1 B. We model all

four possible configurations, henceforth denoted as $1Al_x$ for H bonded to O(x), and find that their enthalpies lie within 10 kJ/mol, with the O(1)-H bond being most stable.

The energetic differences between the different proton positions are small enough and protons move fast compared to typical measurement times[31] to allow a partial occupation of several of the proton positions at the given conditions. We therefore calculated the Gibbs free energy for all four configurations by correcting the enthalpy by zero-point vibrational corrections and finite temperature vibrational and translational contributions to the partition function for all observed frequencies using all wavenumbers larger than 50 cm^{-1}. In the following, we use these energies to calculate the occupational probabilities for the different configurations as

$$P(O(x)) = \frac{e^{-\frac{\Delta G(1Al_x,T)}{kT}}}{Z},$$

where

$$Z = \sum_x e^{\frac{-\Delta G(1Al_x,T)}{kT}}$$

is the partition function with summation over all possible proton positions x, $\Delta G(1Al_x,T)$ is the Gibbs free energy difference between configuration $1Al_x$ and the most stable 1Al configuration, k is the Boltzmann-constant and T is the temperature. Already at 300 K we see that $1Al_1$ is most stable. ΔG is with up to 15 kJ/mol slightly larger than ΔE, but still, $P(1Al_1)$ is only ~0.85 and also $P(1Al_2)$ and $P(1Al_3)$ are non-zero (displayed in Fig. 2). With increasing temperature, ΔG increases, but the probabilities to find $1Al_2$ and $1Al_3$ and also $1Al_4$ still increase.

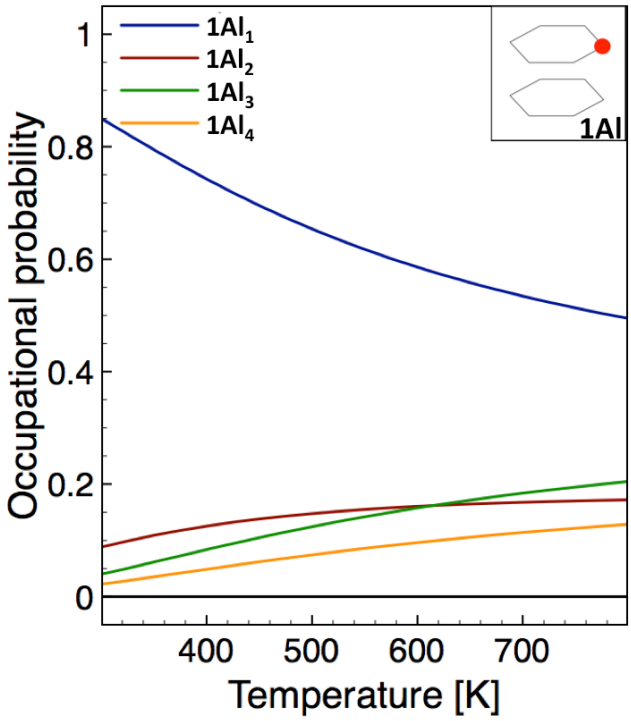

Figure 2: *Occupational probabilities for the 1Al configuration shown in Fig 1 A. Occupational probabilities were calculated using Boltzmann weights; details are given in the main text. Sites with occupations below 0.05 were omitted for clarity.*

The 2 Al case: Next, we focus on the five different possible Al distributions for 2 Al in the unit cell. In this scenario, two different H atoms are placed in the unit cell, which leads to a total of 16 configurations for each of the Al configurations. In the following, they will be denoted as $2Al^{x}{}_{y\text{-}z}$, where x stands for the Al configurations A-E displayed in the respective figures in 1 A and y and z range from 1 to 4 and denote the O atoms to which H atoms are attached, in the vicinity of the two different Al atoms. For all of the Al configurations we follow a similar approach as for the 1 Al case, i.e., we calculate ΔG and the occupational probabilities for them. For all 2 Al configurations we find a larger spread of ΔH and ΔG values compared to the 1 Al

case, but at the same time for all of them several H-positions are accessible at room temperature. The respective occupations depending on the temperature are displayed in Fig. S1. For $2Al^{A}$, $2Al^{D}$ and $2Al^{E}$ we find a dominant H-distribution. However, the behavior with increasing temperature is very different. While the H-distribution becomes more uniform with increased temperature for $2Al^{A}$, the reverse trend is observed for $2Al^{D}$. For $2Al^{E}$ an initial increase in the dominant H-distribution is observed, before it starts dropping again at higher temperature. For $2Al^{B}$ and $2Al^{C}$ a multitude of H-distributions is occupied and no dominant distribution can be identified.

Silanol defects: We furthermore include the possibility of the presence of silanol defects in our model. Here one Al atom is removed and the terminal O atoms are now saturated with hydrogen atoms[32–34]. In all our calculations we find that three OH-groups form a hydrogen-bonded triangle. We therefore consider five scenarios, one case where all four OH groups point towards the center of the removed T-site (furthermore denoted d^4) of the defect and four cases where three OH groups point towards the center of the removed T-site and one OH group points towards the center of the cavity, d^3_X, where X=1-4 (see Fig. 1 C) and denotes the symmetrically different O-atom pointing towards the center of the cavity. In this work we consider two scenarios. First, we focus on a cell volume of 830 $Å^3$. In this scenario, mainly d^4 is occupied at all temperatures (see supporting information section S3). As discussed above, this cell volume is most likely for a zeolite with a medium Si/Al ratio between 5 and 11. However, the possibility of the presence of defects is very important for high Si/Al ratios and avoiding defects during synthesis is a major

issue. We therefore also include calculations for a unit cell volume of 810 $Å^3$, which is close to the unit cell volume of the purely siliceous system. Here, we find a majority occupation for d^3_2 and d^3_1 (see Fig. S2. This massive change with cell volume is rooted in a different minimum unit cell volume of the different defect structures (822.3 $Å^3$ for d^4 vs. 810.3 $Å^3$ for d^3_1). Intuitively such a significant change is understandable, since the lower number of OH bonds pointing towards the empty framework position will reduce the framework stiffness and allow for easier compression. In the discussion below, values for 810 $Å^3$ will be given in the main text, while values for 830 $Å^3$ are given in the supporting information section S3.

OH-IR spectra

So far we have developed a model for the Al position dependent proton distribution in the zeolite SSZ-13. In the course of this work we found that for every Al configuration several proton positions are occupied at finite temperature. As a next step we use this information to calculate OH-IR vibrational spectra and compare them to experimental measurements.

Experimental measurements: As a first step we measured OH-IR spectra for three different SSZ-13 samples with Si/Al ratios of 6 (SSZ13(6)), 12 (SSZ13(12)) and 35 (SSZ13(35)). While the first two samples were synthesized with NaOH as synthesis agent[35,36], the SSZ13(35) sample was synthesized using HF as synthesis agent[37]. After synthesis the samples were dehydrated at 400 °C and analyzed in transmission IR. The OH-region of the samples is shown in Fig. 3. In all samples we find a major peak at 3611 cm^{-1} (green line in Fig. 3). When moving to higher Si/Al

ratios, first a shoulder appears at 3587 cm^{-1} (orange line in Fig. 3), which develops into a distinct peak for SSZ13-35. Furthermore a peak at 3734 cm^{-1} (red line in Fig. 3) is present in all three samples and additionally a distinct peak at 3707 cm^{-1} (blue line in Fig. 3) can be found for the SSZ13-35 sample.

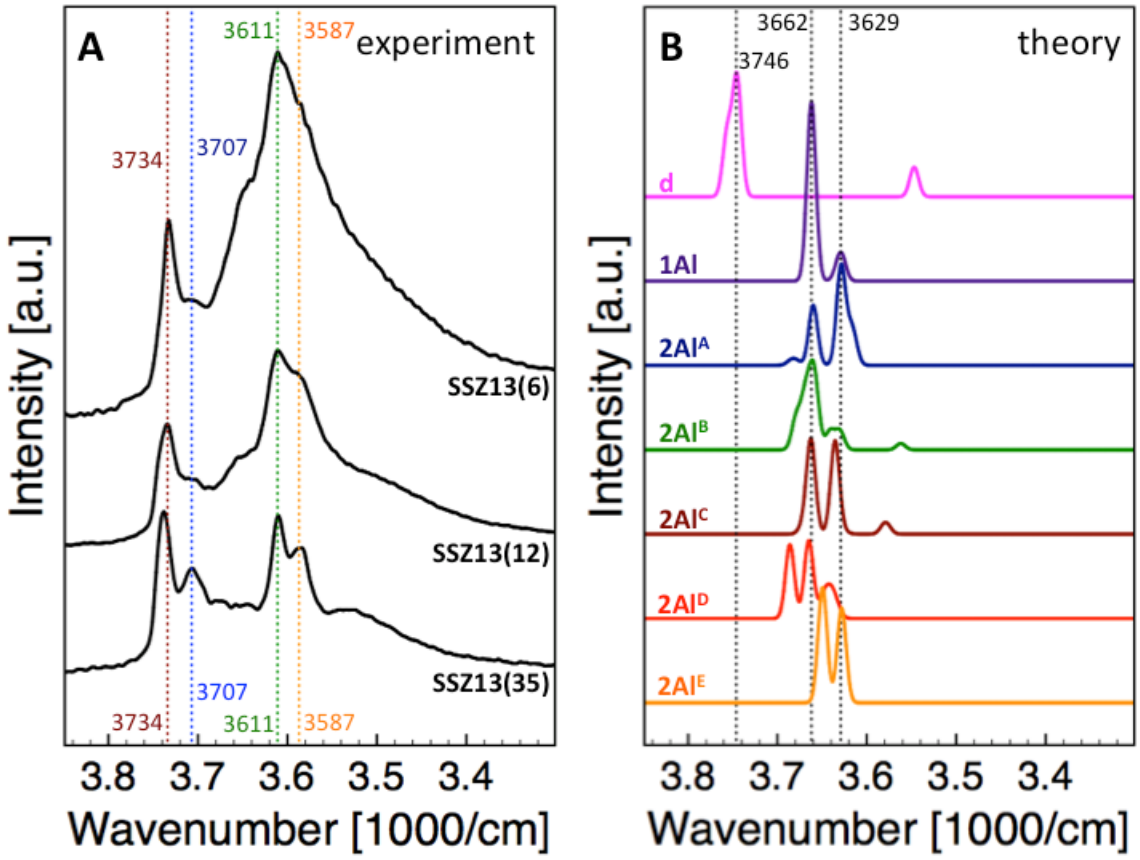

Figure 3: *A: Experimental OH-IR spectrum for three different SSZ-13 samples with different Si/Al ratios (SSZ-13(6), SSZ-13(12), SSZ-13(35)). B: Theoretically calculated OH-IR spectrum at 300 K for the different Al and silanol defect distributions shown in Fig. 1 A. Main spectral features are marked by dashed lines and numerical values indicate the position in* cm^{-1}.

Theoretical calculations: To arrive at the theoretically calculated spectrum we used the frozen phonon approach to assign a vibrational frequency to each OH bond.

The full data for all structures is given in the supporting data file in the supporting information. To construct the finite temperature vibrational spectra we add a Gaussian for each configuration centered at the calculated wavenumber with a standard deviation of 4 cm^{-1}, a typical experimental error bar, and the intensity of the occupational probability calculated above. The corresponding spectra at 300 K are shown in Fig 3 B and temperature dependent spectra and the raw data are shown in the Supporting Information Fig. S3. For all structures a multi-peak spectrum is observed. Most of the peaks lie within a narrow range between 3610 cm^{-1} and 3690 cm^{-1}, with many of the Al configurations showing peaks around 3629 cm^{-1} and 3662 cm^{-1}. Only for $2Al^{B}$ and $2Al^{c}$ a weak, significantly red-shifted peak with low intensity is found.

Next, we investigate the IR spectrum of the defect sites. Here every configuration leads to four different OH-IR wavenumbers. However, due to the formed hydrogen bonded network it is expected that not all of these transitions show similar changes in the dipole moment. To account for this phenomenon we calculate the dipole transition moments and find that mainly one vibrational frequency from the $d^{3}{}_{X}$, corresponding to the silanol groups pointing towards the center of the cavity, contributes to the observed intensity (see Fig. S 4 in the Supporting Information). We therefore use a similar approach as mentioned above using only the IR active highest frequencies and the occupational probabilities to arrive at a spectrum at 300 K (see Fig. 3 B). Temperature-dependent spectra and the underlying spectra are given in the supporting information Figure S3; section S4. Interestingly, the spectra change significantly with cell volume. While for 830 $Å^3$ several features between

3567 cm^{-1} and 3628 cm^{-1} appear (see SI section S3), defect sites at a cell volume of 810 $Å^3$ lead to a spectrum with a main peak at 3746 cm^{-1} and a low intensity peak at 3547 cm^{-1}.

Assigning spectral features: Comparing the modeled spectra to experimental measurements we then assign the major peaks found around 3662 cm^{-1} to the experimental peak at 3611 cm^{-1} and the peak at 3629 cm^{-1} to the experimental peak found at 3582 cm^{-1}. Importantly, the separation between the two peaks is reproduced almost perfectly (33 cm^{-1} for theory vs. 29 cm^{-1} in experiment), with errors in total values in a range typical for DFT calculations (51 cm^{-1} and 47 cm^{-1} respectively). Additionally the spectrum of SSZ13(35) is similar to the spectrum of 1Al. This interpretation agrees well with the expectation of well-separated Al atoms for this system[22]. Based on our model, a decrease in Si/Al ratio will lead to an increase in the amount of paired Al configurations, which will lead to a loss of resolution and a broadening of the observed spectra. Even though these trends agree well with experimental measurements, the overlap of the different bands for the modeled sites and the underlying complexity of this system prevent from making a clear assignment of specific local Al distributions based on the experimental spectra.

We furthermore assign the experimentally observed peak at 3707 cm^{-1} to the defect peak modeled at 3746 cm^{-1}. We find reasonably good agreement in relative shifts with respect to the IR bands associated with different Al configurations (117 cm^{-1} and 84 cm^{-1} in modeling and 125 cm^{-1} and 96 cm^{-1} experimentally) and total errors within DFT error range (39 cm^{-1}). This leaves the peak at 3734 cm^{-1}, which we

assign to silanol groups on the outer surface of the nanoparticle. Due to the complexity of potential zeolite surface reconstructions, modeling this peak goes beyond the scope of this work[38], but the similarity of this peak for all three zeolite samples and comparison with the literature justifies this choice.

^{29}Si and ^{27}Al NMR

Another technique that is commonly used in characterizing zeolite materials is NMR spectroscopy. Here the main focus lies on Si and Al, which are the most common building blocks of zeolites and are NMR sensitive. Typical measurements are performed for samples exposed to a standard atmosphere[15–17] and changes for the dehydrated samples have been reported[39]. Here, we measure ^{29}Si and ^{27}Al NMR spectra and use theory to explain the observed isotropic shifts and differences between measurements for dehydrated and hydrated samples.

Experimental measurements: We focus on the three zeolite samples at different Si/Al ratios described in the section on OH-IR measurements and measured ^{29}Si and ^{27}Al NMR spectra in ambient atmosphere. For the ^{29}Si spectra of all three samples we find two signals, namely a main peak at an isotropic chemical shift between -111 ppm and -112 ppm and a side peak at -105 ppm (see Fig. 4 A). The relative intensity of the side peak compared to the main peak decreases with increased Si/Al ratio. Furthermore a clearly pronounced peak at -102 ppm appears for SSZ13(35). Lastly, we measured the signals for the dehydrated materials. While isotropic chemical shifts agree within 1 ppm, the observed peaks are less well resolved. For the ^{27}Al

NMR spectra measured under ambient conditions we find only one isotropic chemical shift for all samples at 60 ppm (see Fig. 4 B). However, in the literature an asymmetry in the ^{27}Al-NMR features for SSZ-13 has been reported by Dedecek et al., who attributed this asymmetry to the presence of two close lying features[40]. To investigate the potential presence of additional features, we compare the main feature of the three different samples (see Fig. S7 in the Supporting Information). Indeed we observe a similar peak shape and a slight asymmetry in the features of SSZ13(12) and SSZ13(35). For SSZ13(6) an even larger broadening is found. Additionally, a peak close to zero chemical shift appears for all samples. At the same time we were not able to measure ^{27}Al NMR spectra for the dehydrated samples, due to a too low signal to noise ratio.

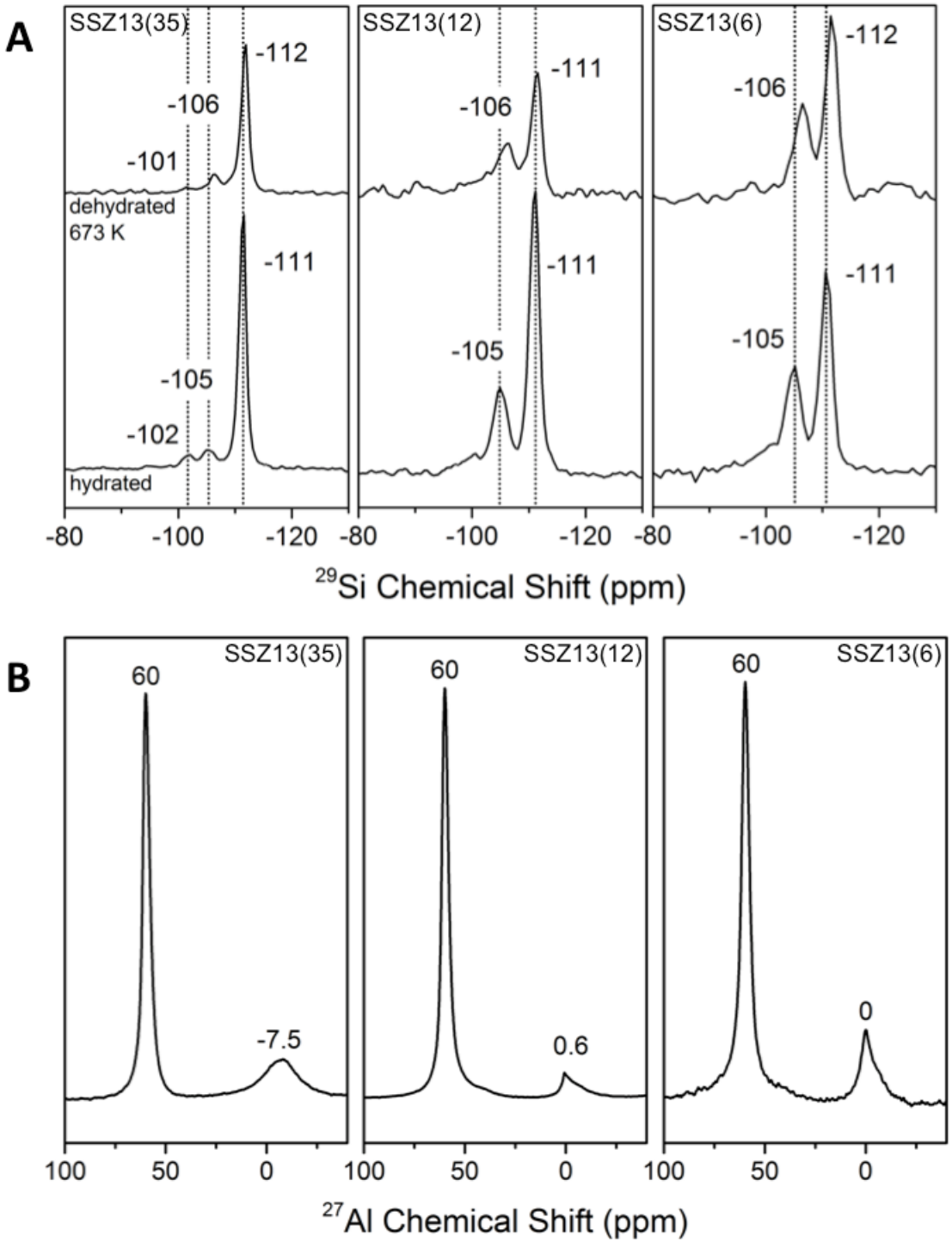

Figure 4: *A: ^{29}Si-NMR spectra for three different SSZ13 samples. Top spectra are for dehydrated samples, bottom spectra for hydrated samples. B: ^{27}Al-NMR shifts for the hydrated SSZ13 samples discussed above.*

Theoretical calculations: To better understand the experimental trends found for NMR measurements, we calculated isotropic chemical shifts for all the different structures in our theoretical model and the numerical values are given in the Supporting data file. This method assigns an isotropic chemical shift to each atom in the unit cell (i.e. 12 isotropic chemical shifts for Si/Al per unit cell). To have a complete model we furthermore included a purely siliceous SSZ-13 and the defect unit cell. Additionally C_Q and η values were calculated for all Al atoms and are provided in the supporting data file.

We first discuss ^{29}Si NMR isotropic chemical shifts (see Fig. 5, the full data is given in the SI). Discussion in the literature attributes isotropic chemical shifts of Si to the number of Si-O-Al bonds[22,37,41,42]. The largest (i.e. most negative) isotropic chemical shifts are attributed to Si atoms surrounded by four Si T-sites. At the same time smallest (i.e. least negative) isotropic chemical shifts have been attributed to Si atoms next to silanol defects or with two Si-O-Al bonds. We therefore focus our discussion on the neighboring Al atoms and on the presence and location of protons surrounding them. Since NMR spectroscopy is a method with high sensitivity to local structure, we find a large spread in isotropic chemical shifts for all different Si coordinations. Calculating isotropic chemical shifts for a situation without protons located at the Si-O-Al bonds, we find that the average isotropic chemical shift changes from -115 ppm (0 Si-O-Al bonds) to -110 ppm (1 Si-O-Al bond) and -105 ppm (2 Si-O-Al bonds), which agrees well with trends in previous assignments in the literature. The situation changes when protons bind to the linking O atoms and the symmetry gets distorted. While the averages only change by a few ppm (-111 ppm

for one Al-OH-Si bond, -107 for 1 Al-OH-Si and one Al-O-Si bond, and -106 ppm for 2 Al-OH-Si), significant differences can be seen for H binding to symmetrically different sites. In general H binding to O(1) leads to the most negative shift, followed by O(3), O(4) and O(2) leading to the least negative isotropic chemical shifts. To complete the picture we also include the values for defects. Values for Si atoms show the largest splits with lowest values of -107 ppm, but highest values of -87 ppm. However, for this analysis we will omit values above -95 ppm, since they are only found for sites that are thermodynamically not accessible under realistic conditions. For the remaining sites we find an average value of -105 ppm.

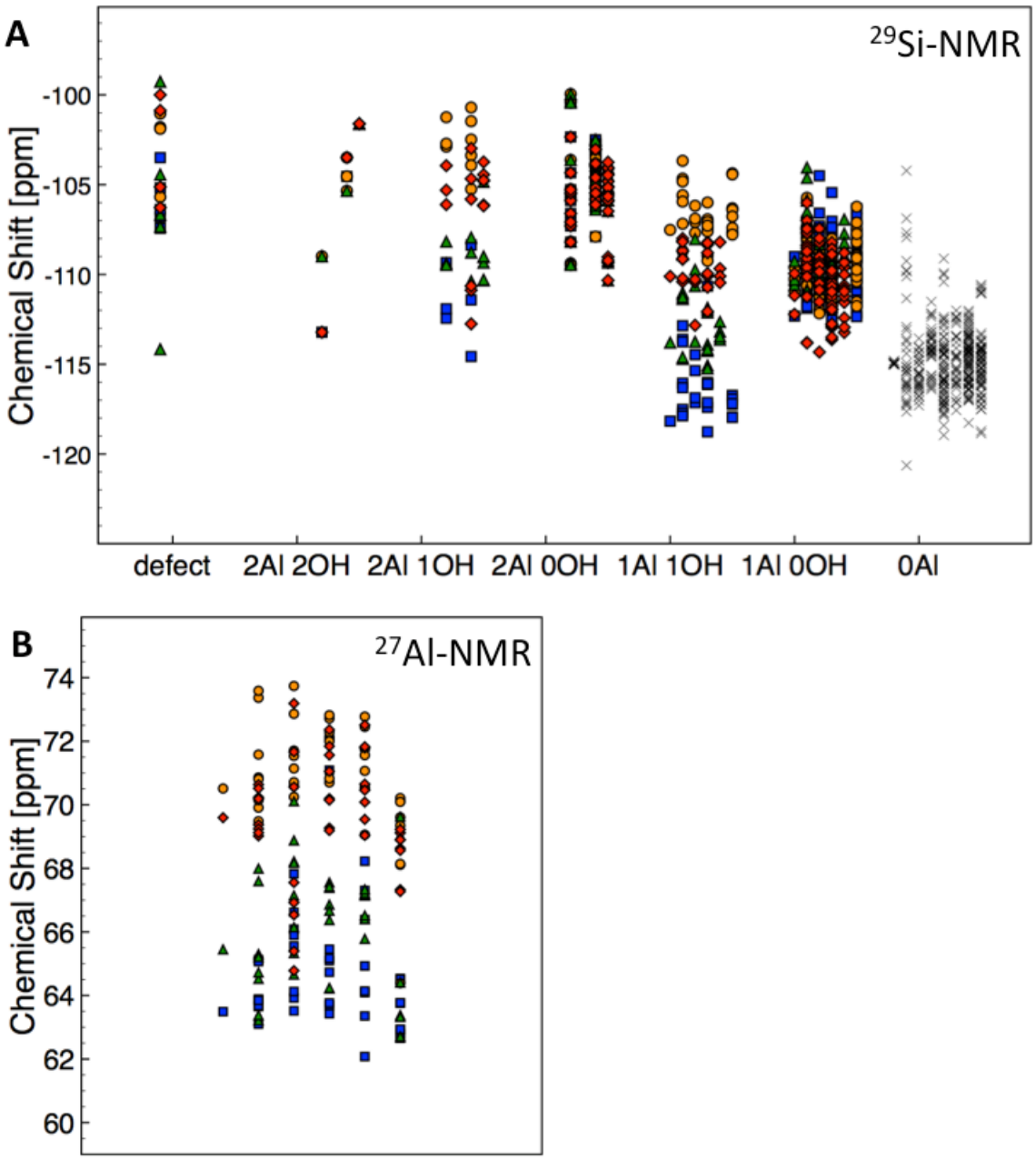

Figure 5: *A: [29]Si-NMR shifts calculated for all modeled zeolite structures. x denote Si forming four Si-O-Si bonds, blue squares show a Si-O(1)-Al bond, orange circles a Si-O(2)-Al bond, green triangles a Si-O(3)-Al bond and red diamonds a Si-O(4)-Al bond. B: [27]Al-NMR shifts for all modeled SSZ13 structures. Blue squares correspond to Al-O(1)H-Si bonds, orange circles to Al-O(2)H-Si bonds, green triangles to Al-O(3)H-Si bonds and red diamonds to Al-O(4)H-Si*

bonds. Columns of data represent (from left to right) Si-SSZ13 (if applicable), d (if applicable), 1Al, 2Al^{A}-2Al^{E}. Numerical values for isotropic chemical shifts are given in the Supporting Information.

Next, we focus on the isotropic chemical shifts of the Al atoms (see Fig. 5 B). The isotropic chemical shifts center around 68 ppm, but at the same time a significant dependence on the location of the proton is found (65 ppm, 71 ppm, 66 ppm, 70 ppm for Al-O(1,2,3,4)H-Si). Using the occupational probabilities calculated above, it is now possible to calculate temperature dependent ^{27}Al NMR spectra. Again, complex multi-peak spectra for each site are found, which change with temperature (see section S5 and Fig. S4 in the supporting information). However, this prediction contradicts the experimental observations of one specific isotropic chemical shift for all three samples.

The impact of ambient conditions: To solve this conundrum we use a method suggested in the literature for calculating NMR spectra[15,16]. Since the system is exposed to an ambient atmosphere, the zeolite is exposed to significant amounts of water. Water in zeolite pores is known to solvate protons[43] and therefore the local strain to the framework caused by the O-H bond is relieved. To appropriately take this phenomenon into account, we model the zeolite without protons and a uniform background charge compensating the charge located at the Al atom. First, we re-optimized the unit cell and find a significant increase in the unit cell volume (see supporting information section S 1), a phenomenon also observed in experimental measurements upon hydration[9]. To take this phenomenon into account we increase the unit cell volume to 860 Å^3.

Indeed we find significant changes in the calculated NMR spectra (see Fig. S6). Averages for ^{29}Si-NMR are now slightly shifted to lower isotropic chemical shifts (-119 ppm for 0 Si-O-Al, -114 ppm for 1 Si-O-Al and -109 ppm for 2 Si-O-Al), but these shifts are generally constant (see Fig. S6 A). More importantly the spread in the values is significantly reduced, which can be attributed to the more symmetric environment surrounding the Si atoms. A similar phenomenon can be found for ^{27}Al-NMR spectra (see Fig. S6 B). Now all spectra fall within 3 ppm, in agreement with a more perfect symmetry surrounding the atoms.

Assigning spectral features: Based on this data it is now possible to assign spectral features observed in experimental measurements. For ^{29}Si-NMR, we assign the feature observed at ~-112 ppm to Si forming four Si-O-Si bonds, the peak at ~-105 ppm to Si forming three Si-O-Si bonds and one Si-O-Al bond. An assignment of the feature at ~-102 ppm is more difficult, since our theoretical data indicates two possibilities, namely an assignment to Si next to a silanol defect or to Si forming two Si-O-Si and two Si-O-Al bonds. However, given the low amount of Al and the chosen synthesis method we are inclined to assign this signal to defect sites. This also agrees with the observation of a defect related peak in the OH-IR spectrum and the conventional interpretation in the literature[8,37,42]. However, our model explains the loss of resolution in ^{29}Si-NMR upon dehydration, which indicates a correlation with the breaking of the symmetry due to the elongation of Si-OH bonds compared to Si-O bonds. This phenomenon is more important for ^{27}Al-NMR, where the almost perfect tetrahedral symmetry around Al atom under ambient conditions makes the NMR spectra collapse into one signal. However, the slight asymmetry observed for

SSZ13(12) and SSZ13(35) indicates the presence of multiple, close lying features. Additionally a further broadening for the SSZ13(6) sample is observed. This behavior is consistent with observations for OH-IR spectra discussed above and can be linked to a distribution of local Al configurations with close lying ^{27}Al-NMR isotropic chemical shifts, which becomes increasingly complex at lower Si/Al ratios. Such an interpretation is supported by modeled ^{27}Al-NMR isotropic shifts, which lie within 3 ppm for all modeled structures. However the complexity of the distribution of Al configurations with close lying isotropic shifts makes an unambiguous assignment difficult. At the same time our model indicates that for a dehydrated sample the Al isotropic chemical shifts should be further separated. Therefore, overcoming complications with signal to noise ratio due to strong quadrupolar coupling might allow to extract more information about this system.

Limitations of the theoretical model:

As we have demonstrated above, the model presented here helps us describe and understand trends observed in OH-IR and NMR spectroscopy in protonated zeolites. At the same time, two major assumptions have been made to allow for the construction of a sufficiently simple model to describe the distribution of Al atoms in a fully periodic framework: (i) all unit cells in a realistic zeolite framework have the same volume and shape and (ii) the interactions between neighboring unit cells are negligible, even if the Al distribution is different. Here we attempt to estimate to which extent these assumptions might influence the different observables.

The impact of the unit cell volume: As already demonstrated for the defect unit cell, the change of unit cell volume can have significant impact on the occupational probabilities. In a realistic zeolite a distribution of unit cells with different local Al configurations and Si/Al ratios will be present, each with a slightly different unit cell shape and volume. Therefore, each unit cell will not be at its equilibrium volume, but at the average volume of the distribution. To assess the impact of a change in cell volume on the occupational probabilities, we first focus on the 1Al site and model the protonated form at 810 $Å^3$. When we now study the occupational probabilities, we see that the majority occupation does not change significantly. However, at higher temperatures changes in the minority occupation ($1Al_4$ over $1Al_2$ and $1Al_3$) start to appear (see Fig. 6 A). To furthermore study the impact of the unit cell volume we focused on the 1Al unit cell. First, we focused on the $1Al_1$ unit cell, varied the volume of the unit cell between 780 $Å^3$ and 870 $Å^3$, optimized the structure and calculated the OH-IR spectra as described above (see Fig. 6 B). We find that the OH-IR spectra at smaller cell volumes are more than 20 cm^{-1} higher than at larger cell volumes and follow an arcuscotangens shape. We performed a similar analysis for the hydrated 1Al unit cell and varied the unit cell volume between 800 $Å^3$ and 880 $Å^3$ and calculated ^{29}Si-NMR (Fig 6 C) and ^{27}Al isotropic chemical shifts (Fig. 6 D). In both cases the NMR shifts move to lower values for increased cell volume. For the ^{29}Si NMR shifts we find that all Si atoms get lowered by ~6 ppm and this shift is similar for all different Si atoms. For the ^{27}Al-NMR spectra this change with 12 ppm is even more pronounced.

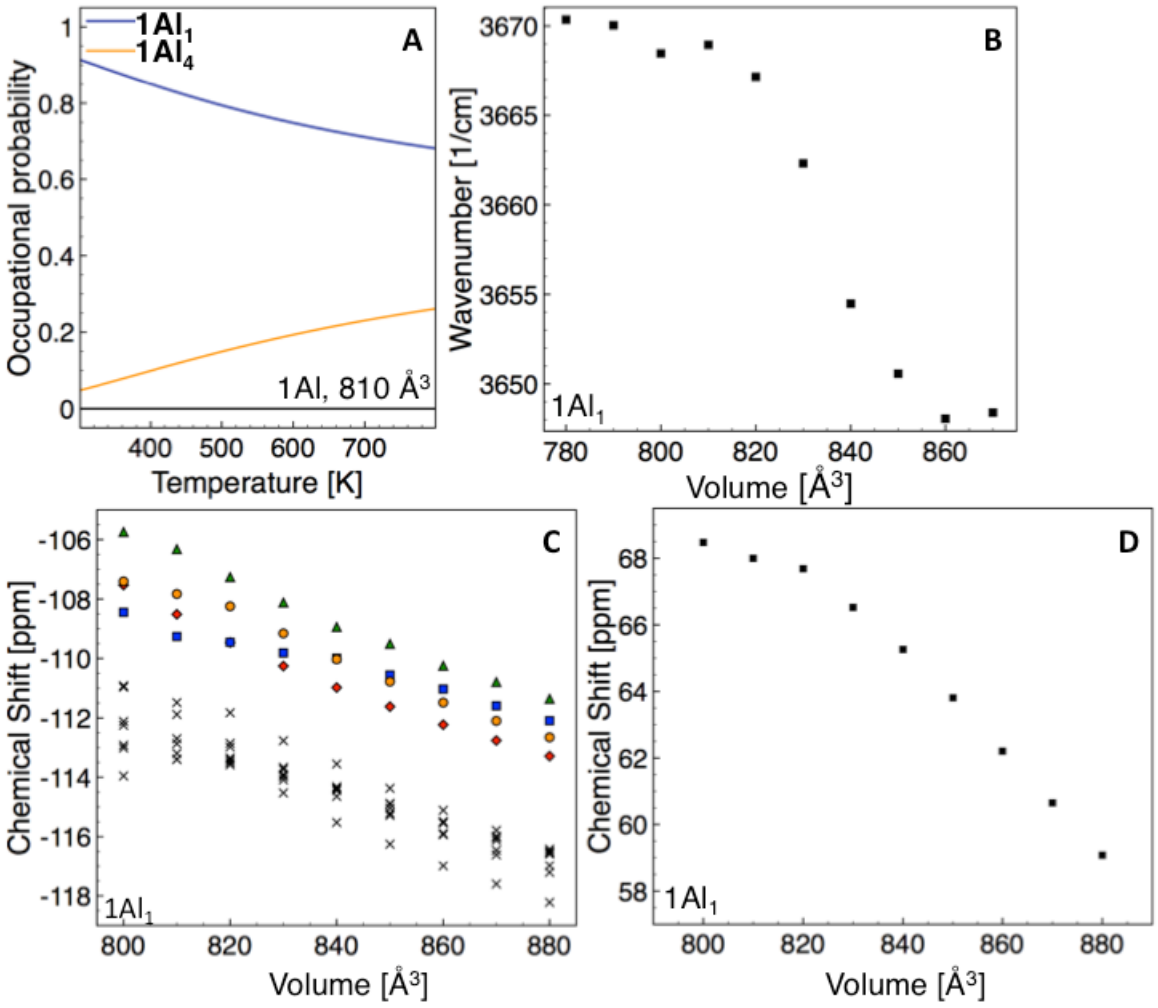

Figure 6: *A: Occupational probabilities calculated for the 1Al site at a volume of 810 Å³. Volume dependence of B the OH-IR spectrum, C the ²⁹Si-NMR spectrum and D the ²⁷Al-NMR spectrum of the 1Al₁ site.* In C *x denotes Si forming four Si-O-Si bonds, blue squares show a Si-O(1)-Al bond, orange circles a Si-O(2)-Al bond, green triangles a Si-O(3)-Al bond and red diamonds a Si-O(4)-Al bond.*

This analysis shows that indeed a dependence of the observables on the unit cell volume exists. However, the changes are comparatively small for NMR spectra when the range of unit cell volumes of a maximum of 30 Å³ is considered. However, for

OH-IR spectra shifts as large as 20 cm^{-1} can be observed in a relatively small cell volume window.

Impact of neighboring unit cells: To evaluate the impact of neighboring unit cells we double the 1Al unit cell and construct three different possible unit cells containing two Al atoms (l^A, l^B and l^C, see Fig. 7 A). The cells are constructed in a way that the total Si/Al ratio of 11 is maintained, but the Al T-sites are only separated by one Si T-site. Using this approach we find that the local Al configuration l^A resembles $2Al^E$, while l^B resembles $2Al^B$, while the local configuration l^C was not included in the initial construction of the model. Subsequently we use a similar methodology as suggested above, i.e. study all possible H positions, and calculate occupational probabilities. All data, and the T-dependent spectra are given in the SI, section S8 and the corresponding OH-IR spectra at 300K are shown in Fig. 7 B. Indeed, the observed spectra change significantly. At the same time the spectrum of l^A reproduces the higher energy peak of $2Al^E$ and the spectrum of l^B is very similar to the spectrum of $2Al^B$.

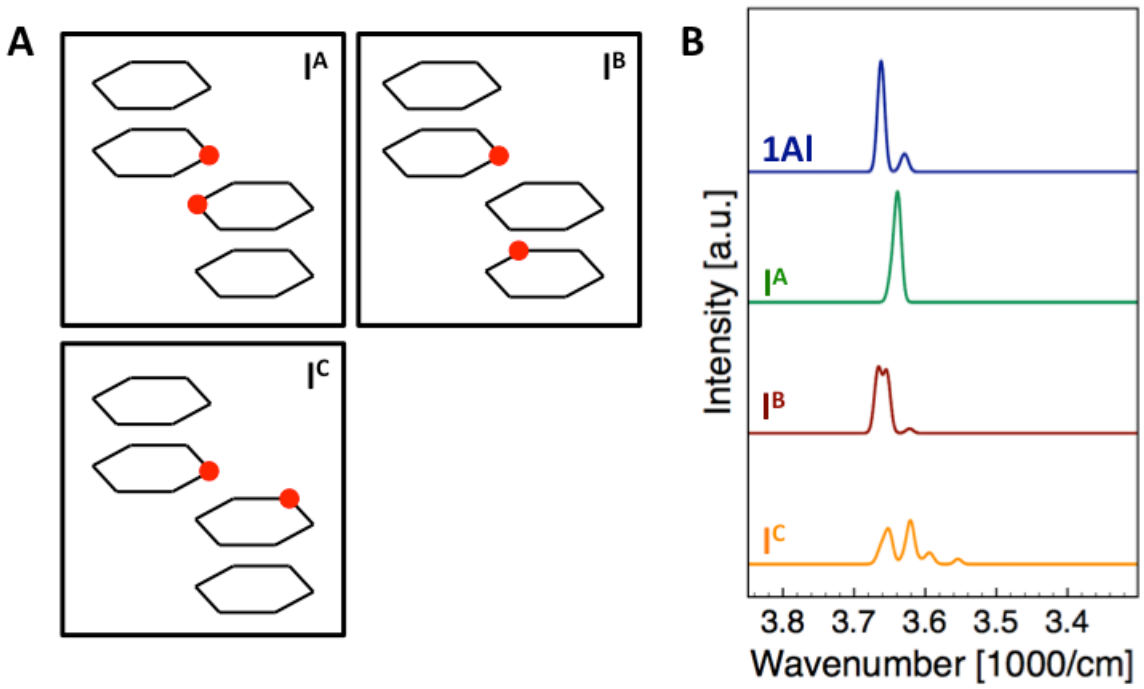

Figure 6: *A: Three different 1Al configurations for a doubled unit cell. Color code corresponds to Fig. 1 A. B: Vibrational spectra calculated for the Al configurations shown in A.*

On one hand these results reveal that the position of Al in neighboring unit cells influences the observed OH-IR spectra. This effect can explain the mismatch observed between the 1Al theoretical spectrum and the SSZ13-35 experimentally measured spectrum and prohibits an exact assignment of features. At the same time trends seem to be captured well, as shown by the calculations in this section. Based on the information presented in this work we expect that OH-IR measurements allow for qualitative assignments of trends in local Al distributions.

Conclusions:

We have developed a coherent model to explain the observed trends in OH-IR, ^{29}Si-NMR and ^{27}Al-NMR spectra for SSZ-13. This model is rooted in the assumption that

in a realistic zeolite a distribution of local Al configurations exists. These local Al configurations are represented by primitive SSZ13 unit cells with the corresponding Al arrangements. In the model discussed here we included unit cells containing zero, one or two Al atoms as well as a framework silanol defect. Subsequently we used Boltzmann occupations to identify the occupational probabilities of different proton positions.

We used the calculated Boltzmann probabilities to construct OH-IR spectra of SSZ13 systems. We find that for each Al configuration distinct multi-peak vibrational spectra are observed. These results allowed us to make assignments in experimental measurements for three different zeolites and indeed the trends for Al configurations and defect sites were reproduced well. Using a similar approach for NMR spectra allowed us to confirm experimental assignments of ^{29}Si-NMR isotropic chemical shifts, but also revealed that distortions in the local symmetry due to the presence of protons lead to a larger spread in observed shifts, which is reflected in a lower resolution in spectra for dehydrated materials. For ^{27}Al-NMR this effect is even more pronounced and makes all observed signals collapse into one signal for all different local configurations.

These results show that the model presented here is successful in describing the general trends in experimental measurements. At the same time assumptions in terms of unit cell volume and the potential impact of stochastic Al distribution on the theoretical side, and the complex, overlapping spectra of different Al configurations are prohibitive to a quantitative assignment. In the future it will be interesting to see how the zeolite model presented here can be extended to other

zeolite structures and to what degree it can be used to obtain insights into various problems in connection with zeolites.

Methods:

Theoretical setup:

All calculations were performed using the Vienna Ab-Initio Simulation Package (VASP)[44,45], a plane wave core using PAW pseudopotentials[46,47]. All calculations were performed using an energy cut-off of 420 eV. In all calculations the k-point sampling was restricted to the Γ-point. The unit cell parameters are reported in the literature[48]. All calculations were carried out using density functional theory in the parameterization of Perdew, Burke and Ernzerhof (PBE)[49]. Vibrational frequencies were calculated using the frozen phonon approach. A short discussion of the impact of the energy cut-off is given in supporting information section S10. Temperature corrections were calculated using the code thermo.pl[50], a code provided by the National Institute of Standards and Technology and only frequencies higher than 50 cm^{-1} were considered in the analysis. NMR isotropic chemical shifts were calculated for the optimized structures using linear response theory[51,52] as implemented in VASP. Isotropic chemical shifts are reported with respect to tetra methyl silane (TMS) and $Al(H_2O)_6$. Calculations for the reference compounds were carried out in a 10 Å x10 Å x10 Å box.

Experimental methods:

Zeolite Synthesis: SSZ-13 zeolites with Si/Al ratios 6 (SSZ-13-6) and 12 (SSZ-13-12) were synthesized following a procedure described elsewhere.[53] For the preparation

of the synthesis gel NaOH (0.19 g, ≥97%, Sigma-Aldrich) was dissolved in deionized water (23.5 g) followed by the addition of the structure directing agent TMAda-OH (3.89 g, 25%, SACHEM ZeoGen 2825). After dissolving aluminum hydroxide (0.12 g, 50-5% Al_2O_3, Sigma-Aldrich), fumed silica powder (2.75 g, 0.007 μm average particle size, Sigma-Aldrich) was added under vigorous stirring until a homogeneous gel was observed. The gel with a molar composition of 10 SDA : 10 NaOH : 8.33 Al_2O_3 : 100 SiO_2 : 2200 H_2O for SSZ-13-6 and a molar composition of 10 SDA : 10 NaOH : 4.17 Al_2O_3 : 100 SiO_2 : 2200 H_2O for SSZ-13-12 was then transferred into a 45 mL Teflon-lined stainless steel autoclave, before hydrothermal crystallization was carried out at 160° C in a rotating oven at 60 rpm. After the synthesis the solid was recovered by filtration and washed with deionized water and acetone. Finally the zeolite powder was dried in a convection oven at 110° C and calcined at 650° C for 6h with a ramp of 3° C/min under an air flow. To transform the Na form of the SSZ-13 (Na-SSZ-13-OH) into its protonic form (H-SSZ-13-OH) the zeolite was ion-exchanged in 3 cycles with a 1 M ammonium nitrate solution at 80° C for 12h. After each cycle the zeolite was filtered, washed with water and dried at 110° C over night. After the final exchange the sample was subjected to an additional calcination step at 580° C for 6h under an air flow. The Si/Al ratios of 6 and 12 were confirmed by ICP-AES.

The Si/Al=35 sample was prepared by adapting the method reported by Eilertsen *et al.*[37]. Al powder (0.05 g, 99.99%, Acros) was dissolved in TMAda-OH solution (26.6 g, 25%, SACHEM, ZeoHen 2825). After complete dissolution a mixture of Ethanol (8 g, 200 Proof) and tetraethyl-orthosilicate (13 g, TEOS, 98%, Sigma-Aldrich) was

added dropwise. After hydrolysis of the TEOS the synthesis gel was heated up to 50° C under stirring to evaporate excess of water. The resulting mixture was ground prior to the dropwise addition of hydrofluoric acid (1.28 g, 48 wt%, Sigma-Aldrich). Homogeneity was ensured by mixing with a PTFE spatula. The final synthesis gel with the composition 50 SDA:50 HF:1.43 Al_2O_3:100 SiO_2:300 H_2O was then charged into a Teflon-lined stainless steel autoclave and hydrothermal crystallization was carried out at 155° C for 7 days in a rotating oven (60 rpm). The crystalline product was collected by filtration and washed with deionized water and acetone before drying it at 110° C. To remove the SDA the material was calcined at 600° C for 6h under an air flow. The Si/Al ratios of all materials were confirmed by ICP-AES. The crystal structure of the materials was confirmed using Powder X-Ray Diffraction.

Transmission FTIR: Prior to analysis, samples were dehydrated at 400 °C (10 °C min^{-1}) under a flow of nitrogen. IR analysis was carried out in a N_2 glovebox (<1 ppm O_2 and H_2O) to prevent readsorption of water during analysis. Samples were suspended in KBr and pressed into self-supporting wafers, then analyzed via transmission IR (Bruker Alpha spectrometer), each with 16 scans at a resolution of 4 cm^{-1}. All spectra were baseline corrected and normalized to the intensity of the Si-O-Si overtones.

Solid state NMR: Solid-state ^{29}Si-NMR and ^{27}Al-NMR spectra were acquired on an Avance III NMR spectrometer (Bruker) operating at a ^{1}H Larmor frequency of 500 MHz. The samples were spun around the Magic Angle with a rate of 15 kHz at room temperature using air for the drive, bearing and VT flow. A 4 mm probe was tuned to 99.362 MHz or 130.32 MHz for the ^{29}Si and ^{27}Al experiments respectively. The

ppm scale of the spectra was calibrated using the ^{29}Si and ^{27}Al signals of kaolinite as an external secondary reference (-91.5 ppm and 0 ppm, respectively)[54]. Samples dehydrated under N_2 at 400 °C were packed into rotors inside a glovebox (< 1ppm O_2 and H_2O).

Acknowledgements: F. Göltl and M. Mavrikakis acknowledge support from the National Science Foundation, grant number CHE-1800284. The authors acknowledge computational time at the National Energy Research Scientific Computing Center (NERSC), a DOE Office of Science User Facility supported by the Office of Science of the U.S. Department of Energy, contract DE-AC02-05CH11231, under Project No. mp-351 and Phoenix Supercomputer, which is supported in part by National Science Foundation Grant CHE-0840494. This research was in part performed using the computing resources and assistance of the UW-Madison Center for High Throughput Computing (CHTC) in the Department of Computer Sciences. The CHTC is supported by UW-Madison, the Advanced Computing Initiative, the Wisconsin Alumni Research Foundation, the Wisconsin Institutes for Discovery, and the National Science Foundation, and is an active member of the Open Science Grid, which is supported by the National Science Foundation and the U.S. Department of Energy's Office of Science. This study made use of the National Magnetic Resonance Facility at Madison, which is supported by NIH grant P41GM103399 (NIGMS), old number: P41RR002301. Equipment was purchased with funds from the University of Wisconsin-Madison, the NIH P41GM103399, S10RR02781, S10RR08438, S10RR023438, S10RR025062, S10RR029220), the NSF (DBI-8415048, OIA-

9977486, DBI-9214394), and the USDA. NMR studies were supported by funds from NIH shared instrumentation grant S10RR027000 and the University of Wisconsin-Madison.

Supporting information: The supporting information contains information on the choice of cell volume, occupational probabilities for the 2Al configurations and the silanol defect, data for the silanol defect unit cell at a volume of 830 $Å^3$, temperature dependent OH-IR spectra, a discussion on IR active frequencies for the silanol defect sites, temperature dependent ^{27}Al-NMR spectra, ^{27}Al-NMR and ^{29}Si-NMR chemical shifts for all unit cells, magnified ^{27}Al-NMR spectra for the hydrated zeolite samples, information on calculations in the large unit cell and data for the impact of a higher energy cut-off. Furthermore a data file containing the raw data and all optimized structures at 830 $Å^3$ are included.

References:

1 R. Gounder and E. Iglesia, The catalytic diversity of zeolites: confinement and solvation effects within voids of molecular dimensions., *Chem. Commun. (Camb).*, 2013, **49**, 3491–509.

2 F. Göltl, C. Michel, P. C. Andrikopoulos, A. M. Love, J. Hafner, I. Hermans and P. Sautet, Computationally Exploring Confinement Effects in the Methane-to-Methanol Conversion Over Iron-Oxo Centers in Zeolites, *ACS Catal.*, 2016, **6**, 8404–8409.

3 M. Boronat, C. Martinez and A. Corma, Mechanistic differences between methanol and dimethyl ether carbonylation in side pockets and large channels of mordenite, *Phys. Chem. Chem. Phys.*, 2011, **13**, 2603–2612.

4 S. Conrad, R. Verel, C. Hammond, P. Wolf, F. Göltl and I. Hermans, Silica-Grafted Sn ^{IV} Catalysts in Hydrogen-Transfer Reactions, *ChemCatChem*, 2015, **7**, 3270–3278.

5 F. Göltl, R. Bulo, J. Hafner, P. Sautet, F. Göltl and R. Bulo, What Makes Copper-Exchanged SSZ-13 Zeolite Efficient at Cleaning Car Exhaust Gases?, *J. Phys. Chem. Lett.*, 2013, **4**, 2244–2249.

6 F. Göltl, P. Müller, P. Uchupalanun, P. Sautet and I. Hermans, Developing a Descriptor-Based Approach for CO and NO Adsorption Strength to Transition Metal Sites in Zeolites, *Chem. Mater.*, 2017, **29**, 6434–6444.

7 S. Nystrom, A. Hoffman and D. Hibbitts, Tuning Brønsted Acid Strength by Altering Site Proximity in CHA Framework Zeolites, *ACS Catal.*, 2018, **8**, 7842–7860.
8 J. R. Di Iorio, C. T. Nimlos and R. Gounder, Introducing Catalytic Diversity into Single-Site Chabazite Zeolites of Fixed Composition via Synthetic Control of Active Site Proximity, *ACS Catal.*, 2017, **7**, 6663–6674.
9 B. Ipek, M. J. Wulfers, H. Kim, F. Göltl, I. Hermans, J. P. Smith, K. S. Booksh, C. M. Brown and R. F. Lobo, Formation of $[Cu_2O_2]^{2+}$ and $[Cu_2O]^{2+}$ toward C-H Bond Activation in Cu-SSZ-13 and Cu-SSZ-39, *ACS Catal.*, 2017, **7**, 4291–4303.
10 C. Paolucci, A. A. Parekh, I. Khurana, J. R. Di Iorio, H. Li, J. D. Albarracin Caballero, A. J. Shih, T. Anggara, W. N. Delgass, J. T. Miller, F. H. Ribeiro, R. Gounder and W. F. Schneider, Catalysis in a cage: Condition-dependent speciation and dynamics of exchanged cu cations in ssz-13 zeolites, *J. Am. Chem. Soc.*, 2016, **138**, 6028–6048.
11 W. Loewenstein, The Distribution fo Aluminum in the tetrahedra of silicates and aluminates, *Am. Mineral.*, 1954, **39**, 92–96.
12 A. Alberti, G. Gottardi, I. Mineralogia, U. Modena and V. S. Eufemia, The determination of the Al-content in the tetrahedra of framework silicates, *Zeitschrift für Krist.*, 1988, **184**, 49–61.
13 G. Sastre, V. Fornes and A. Corma, On the preferential location of Al and proton siting in zeolites: A computational and infrared study, *J. Phys. Chem. B*, 2002, **106**, 701–708.
14 P. Losch, H. R. Joshi, O. Vozniuk, A. Grünert, C. Ochoa-Hernández, H. Jabraoui, M. Badawi and W. Schmidt, Proton Mobility, Intrinsic Acid Strength, and Acid Site Location in Zeolites Revealed by Varying Temperature Infrared Spectroscopy and Density Functional Theory Studies, *J. Am. Chem. Soc.*, 2018, **140**, 17790–17799.
15 J. Dedecek, M. J. Lucero, C. Li, F. Gao, P. Klein, M. Urbanova, Z. Tvaruzkova, P. Sazama and S. Sklenak, Complex analysis of the aluminum siting in the framework of silicon-rich zeolites. A case study on ferrierites, *J. Phys. Chem. C*, 2011, **115**, 11056–11064.
16 S. Sklenak, J. Dědeček, C. Li, B. Wichterlová, V. Gábová, M. Sierka and J. Sauer, Aluminum siting in silicon-rich zeolite frameworks: A combined high-resolution ^{27}Al NMR spectroscopy and quantum mechanics/molecular mechanics study of ZSM-5, *Angew. Chemie - Int. Ed.*, 2007, **46**, 7286–7289.
17 J. Dědeček, Z. Sobalík and B. Wichterlová, Siting and Distribution of Framework Aluminium Atoms in Silicon-Rich Zeolites and Impact on Catalysis, *Catal. Rev.*, 2012, **54**, 135–223.
18 K. Mlekodaj, J. Dedecek, V. Pashkova, E. Tabor, P. Klein, M. Urbanova, R. Karcz, P. Sazama, S. R. Whittleton, H. M. Thomas, A. V Fishchuk and S. Sklenak, Al Organization in the SSZ-13 Zeolite . Al Distribution and Extraframework Sites of Divalent Cations, *J. Phys. Chem. C*, 2019, **123**, 7968–7987.
19 J. A. van Bokhoven, T. Lee, M. Drakopoulos, C. Lamberti, S. Thieß and J. Zegenhagen, Determining the aluminium occupancy on the active T-sites in zeolites using X-ray standing waves, *Nat. Mater.*, **4**, 551–555.
20 F. Göltl, P. Sautet and I. Hermans, Can Dynamics Be Responsible for the

Complex Multipeak Infrared Spectra of NO Adsorbed to Copper(II) Sites in Zeolites?, *Angew. Chemie - Int. Ed.*, 2015, **54**, 7799–7804.
21 F. Göltl, A. M. Love and I. Hermans, Developing a Thermodynamic Model for the Interactions Between Water and Cu in the Zeolite SSZ-13, *J. Phys. Chem. C*, 2017, **121**, 6160–6169.
22 J. R. Di Iorio and R. Gounder, Controlling the Isolation and Pairing of Aluminum in Chabazite Zeolites Using Mixtures of Organic and Inorganic Structure-Directing Agents, *Chem. Mater.*, 2016, **28**, 2236–2247.
23 A. M. Beale, F. Gao, I. Lezcano-Gonzalez, C. H. F. Peden and J. Szanyi, Recent advances in automotive catalysis for NO_x emission control by small-pore microporous materials, *Chem. Soc. Rev.*, 2015, **44**, 7371–7405.
24 C. Paolucci, J. R. Di Iorio, F. . Ribeiro, R. Gounder and W. F. Schneider, in *Advances in Catalysis*, Elsevier Inc., 1st edn., 2016, vol. 59, pp. 1–107.
25 K. Narsimhan, K. Iyoki, K. Dinh and Y. Román-Leshkov, Catalytic Oxidation of Methane into Methanol over Copper-Exchanged Zeolites with Oxygen at Low Temperature, *ACS Cent. Sci.*, 2016, **2**, 424–429.
26 B. Ipek and R. F. Lobo, Catalytic conversion of methane to methanol on Cu-SSZ-13 using N_2O as oxidant, *Chem. Commun.*, 2016, **5**, 1668–1686.
27 T. Takaishi, M. Kato and K. Itabashi, Stability of the Al-O-Si-O-Al Linkage in Zeolititc Framework, *J. Phys. Chem.*, 1994, **98**, 5742–5743.
28 T. Takaishi, M. Kato and K. Itabashi, Determination of the ordered distribution of aluminum atoms in a zeolitic framework , Part II, *Zeolites*, 1995, **15**, 21–32.
29 F. Göltl, P. Sautet and I. Hermans, The impact of finite temperature on the coordination of Cu cations in the zeolite SSZ-13, *Catal. Today*, 2016, **267**, 41–46.
30 F. Göltl and J. Hafner, Structure and properties of metal-exchanged zeolites studied using gradient-corrected and hybrid functionals. I. Structure and energetics, *J. Chem. Phys.*, 2012, **136**, 064501.
31 M. Sierka and J. Sauer, Proton Mobility in Chabazite , Faujasite , and ZSM-5 Zeolite Catalysts . Comparison Based on ab Initio Calculations, 2001, **5**, 1603–1613.
32 M. Nielsen, R. Y. Brogaard, H. Falsig, P. Beato, O. Swang and S. Svelle, Kinetics of Zeolite Dealumination: Insights from H-SSZ-13, *ACS Catal.*, 2015, **5**, 7131–7139.
33 M. Silaghi, E. Petracovschi, T. Kerber, J. Sauer and P. Raybaud, Regioselectivity of Al − O Bond Hydrolysis during Zeolites Dealumination Uni fi ed by Brønsted − Evans − Polanyi Relationship, *ACS Catal.*, 2015, **5**, 11–15.
34 M. C. Silaghi, C. Chizallet, J. Sauer and P. Raybaud, Dealumination m echanisms of zeolites and extra-framework aluminum confinement, *J. Catal.*, 2016, **339**, 242–255.
35 S. I. Zones, Conversion of faujasites to high-silica chabazite SSZ-13 in the presence of N,N,N-trimethyl-1-adamantammonium iodide, *J. Chem. Soc. Faraday Trans.*, 1991, **87**, 3709–3716.
36 D. W. Fickel and R. F. Lobo, Copper coordination in Cu-SSZ-13 and Cu-SSZ-16 investigated by variable-temperature XRD, *J. Phys. Chem. C*, 2010, **114**, 1633–1640.

37 E. A. Eilertsen, B. Arstad, S. Svelle, K. P. Lillerud and S. Al, Microporous and Mesoporous Materials Single parameter synthesis of high silica CHA zeolites from fluoride media, *Microporous Mesoporous Mater.*, 2012, **153**, 94–99.
38 J. Rey, P. Raybaud and C. Chizallet, Ab Initio Simulation of the Acid Sites at the External Surface of Zeolite Beta, *ChemCatChem*, 2017, **9**, 2176–2185.
39 P. Klein, V. Pashkova, H. M. Thomas, S. R. Whittleton, J. Brus, L. Kobera, J. Dedecek and S. Sklenak, Local Structure of Cationic Sites in Dehydrated Zeolites Inferred from27Al Magic-Angle Spinning NMR and Density Functional Theory Calculations. A Study on Li-, Na-, and K-Chabazite, *J. Phys. Chem. C*, 2016, **120**, 14216–14225.
40 J. Dedecek, S. Sklenak, C. Li, F. Gao, J. Brus, Q. Zhu and T. Tatsumi, Effect of Al / Si Substitutions and Silanol Nests on the Local Geometry of Si and Al Framework Sites in Silicone-Rich Zeolites : A Combined High Resolution 27 Al and 29 Si NMR and Density Functional Theory / Molecular Mechanics Study, *J. Phys. Chem. C*, 2009, **113**, 14454–14466.
41 E. Lam, A. Comas-Vives and C. Copéret, Role of Coordination Number, Geometry, and Local Disorder on27Al NMR Chemical Shifts and Quadrupolar Coupling Constants: Case Study with Aluminosilicates, *J. Phys. Chem. C*, 2017, **121**, 19946–19957.
42 S. Prasad and M. Petrov, Mixed domain models for the distribution of aluminum in high silica zeolite SSZ-13, *Solid State Nucl. Magn. Reson.*, 2013, **54**, 26–31.
43 L. Zhu, K. Seff, D. H. Olson, B. J. Cohen and R. B. Von Dreele, Hydronium Ions in Zeolites. 1. Structures of Partially and Fully Dehydrated Na,H_3O–X by X-ray and Neutron Diffraction, *J. Phys. Chem. B*, 1999, **103**, 10365–10372.
44 G. Kresse and J. Hafner, Ab initio molecular dynamics for open-shell transition metals, *Phys. Rev. B*, 1993, **48**, 13115–13118.
45 G. Kresse and J. Furthmüller, Efficiency of ab-initio total energy calculations for metals and semiconductors using a plane-wave basis set, *Comput. Mater. Sci.*, 1996, **6**, 15–50.
46 P. E. Blöchl, Projector augmented-wave method, *Phys. Rev. B*, 1994, **50**, 17953–17979.
47 G. Kresse and D. Joubert, From ultrasoft pseudopotentials to the projector augmented-wave method, *Phys. Rev. B*, 1999, **59**, 1758–1775.
48 F. Göltl and J. Hafner, Structure and properties of metal-exchanged zeolites studied using gradient-corrected and hybrid functionals. III. Energetics and virational spectroscopy of adsorbates, *J. Chem. Phys.*, 2012, **136**, 064503.
49 J. P. Perdew, K. Burke and M. Ernzerhof, Generalized Gradient Approximation Made Simple, *Phys. Rev. Lett.*, 1996, **77**, 3865–3868.
50 K. K. Irikura, Thermo.pl, *Natl. Inst. Stand. Technol.*
51 C. J. Pickard and F. Mauri, All-electron magnetic response with pseudopotentials: NMR chemical shifts, *Phys. Rev. B*, 2001, **63**, 245101.
52 J. R. Yates, C. J. Pickard and F. Mauri, Calculation of NMR chemical shifts for extended systems using ultrasoft pseudopotentials, *Phys. Rev. B - Condens. Matter Mater. Phys.*, 2007, **76**, 1–11.
53 U. Deka, A. Juhin, E. a Eilertsen, H. Emerich, M. a Green, S. T. Korhonen, B. M.

Weckhuysen and A. M. Beale, Confirmation of Isolated Cu^{2+} Ions in SSZ-13 Zeolite as Active Sites in NH_3-Selective Catalytic Reduction., *J. Phys. Chem. C*, 2012, **116**, 4809–4818.

54 J. Rocha and J. Klinowski, ^{29}Si and ^{27}Al Magic-angle-spinning NMR Studies of the Thermal Transformation of Kaolinite, *Phys. Chem. Mater.*, 1990, **17**, 179–186.

Graphical TOC:

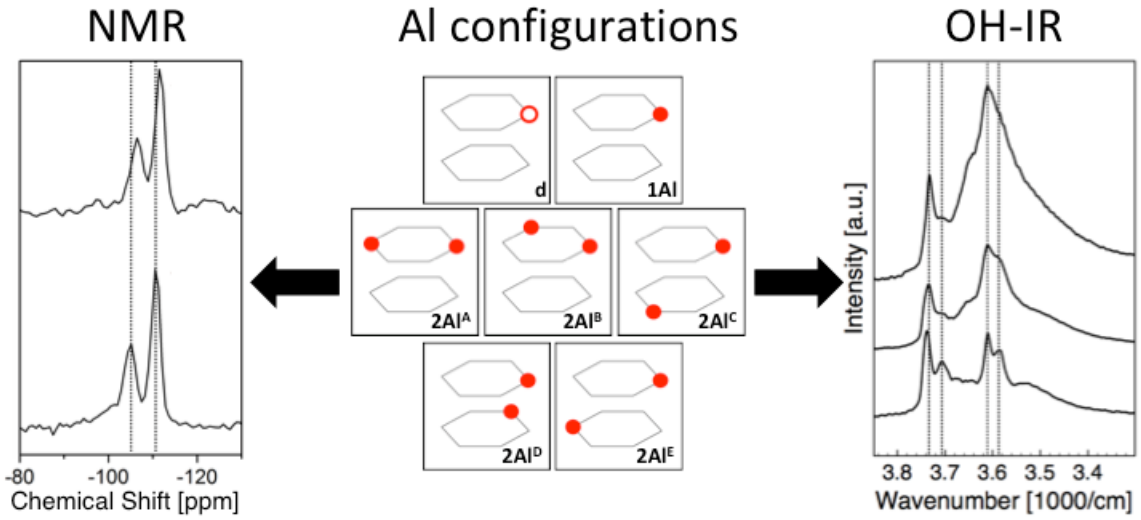

A theoretical model for protonated SSZ13 is used to explain experimentally measured OH-IR vibrational spectra and ^{27}Al-NMR and ^{29}Si-NMR spectra.

Supporting information for

Computational Description of Key Spectroscopic Features of Zeolite SSZ-13

Florian Göltl[1,2,], Alyssa M Love[1], Sarah C. Schuenzel[2], Patrick Wolf[1], Manos Mavrikakis[2,*], Ive Hermans[1,2,*]*

[1] Department of Chemistry, University of Wisconsin – Madison, 53706 Madison, WI, USA Department of Chemical and Biological Engineering, University of Wisconsin – Madison, 53706 Madison, WI, USA

[2] Department of Chemical and Biological Engineering, University of Wisconsin – Madison, 53706 Madison, WI, USA

e-Mail: fgoeltl@wisc.edu, emavrikakis@wisc.edu, hermans@chem.wisc.edu

S1: Choice of cell volume

The protonated case: As a first step we optimize the cell volume for all the studied sites. We systematically varied the unit cell volume over a range from 770 Å^3 and 870 Å^3 and used a square fit to determine the minimum (see Table S1). We find a significant dependence of the different Al and defect distributions. The cell volume in general increases with the Amount of Al in the unit cell (811 Å^3 for 0Al, 823.8 Å^3 for 1Al and ~837 Å^3 for 2Al). Furthermore the defect site is also at a volume of 822.3 Å^3. These values agree reasonably well with reports in the literature and small differences are expected due to differences in the computational setup. If the zeolite would be perfectly periodic and would only consist of one type of unit cell, the choice of unit cell volume would be simple. However, in a realistic zeolite system a distribution of local Al and defect configurations will be present and the unit cell volume will most likely be an average over the Al configurations present. Since most of the work for SSZ-13 focuses on materials with Si/Al ratios above 6 and below 15, we make a compromise and choose a unit cell volume of 830 Å^3 in all our calculations. However, the real unit cell volume might change based on the Si/Al ratio and it might be necessary to adapt the chosen unit cell volume.

Table S1: *Optimized unit cell volume for protonated Al configurations in SSZ-13*.

Site	Volume [Å^3]
Si-SSZ13	811
$1Al_1$	823.8
$2Al^A{}_{1\text{-}1}$	840.6
$2Al^B{}_{1\text{-}1}$	837.7
$2Al^C{}_{2\text{-}1}$	837.5
$2Al^D{}_{1\text{-}1}$	836.8
$2Al^E{}_{1\text{-}1}$	833.0
d^4	822.3
$d^3{}_2$	810.3

Unit cell volumes for a uniform background charge: In a subsequent step we optimized unit cell volumes for systems with a uniform background charge used for NMR calculations. Now we vary the cell volume between 800 Å^3 and 900 Å^3. For all sites we find a significant expansion to 836.5 Å^3 for 1Al and ~862 Å^3 for the 2 Al cases. This expansion is consistent with experimental measurements, which find an expansion of the unit cell volume upon hydration. Following a similar logic as above, we choose a unit cell volume of 860 Å^3.

Table S2: *Optimized unit cell volumes for Al configurations with a uniform background charge*.

Site	Volume [Å^3]
1Al	836.5
2Al^A	862.8
2Al^B	862.4
2Al^C	861.5
2Al^D	863.6
2Al^E	862.7

S2: Occupational probabilities for $2Al^{A}$-$2Al^{E}$ and d

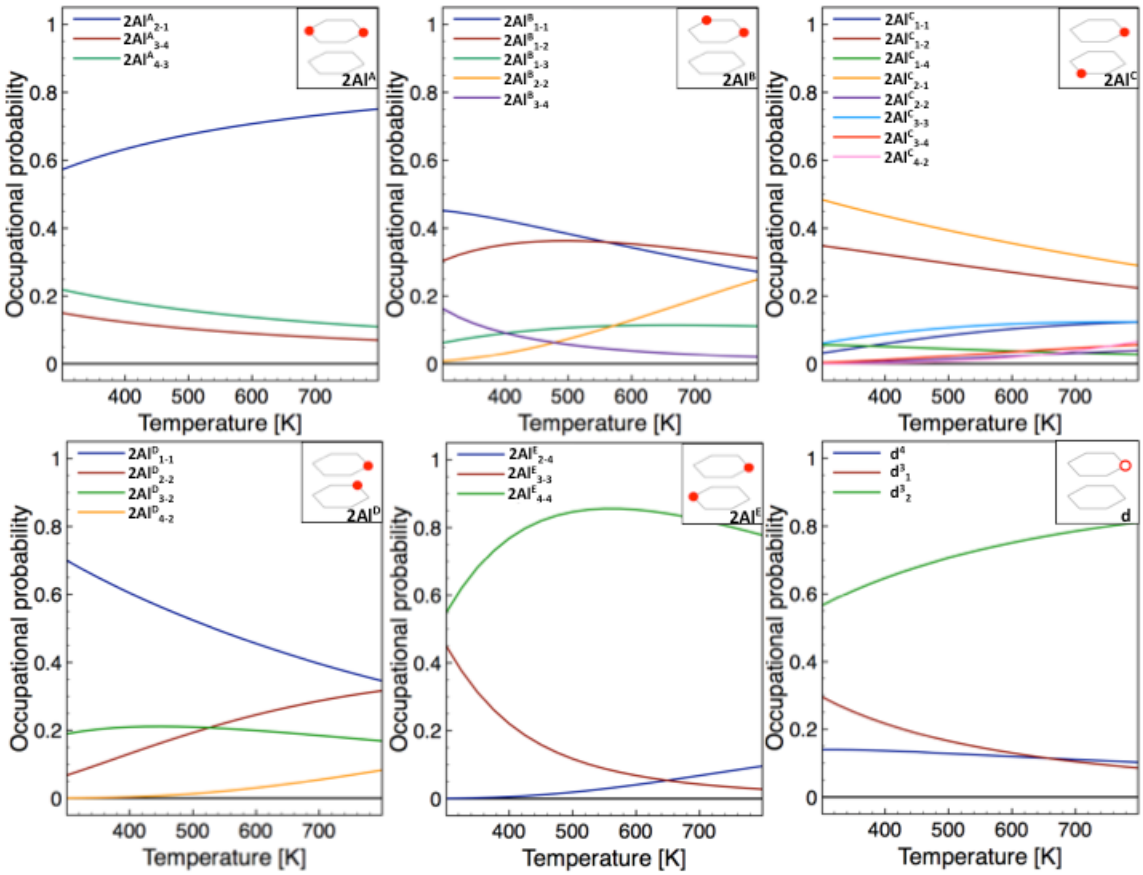

Figure S1: *Occupational probabilities for Al configurations $2Al^{A}$ through $2Al^{E}$ and d as shown in Fig 1 A. Occupational probabilities were calculated using Boltzmann weights; details are given in the main text. Sites with occupations below 0.05 were omitted for clarity.*

S3: Defect sites at 830 Å^3

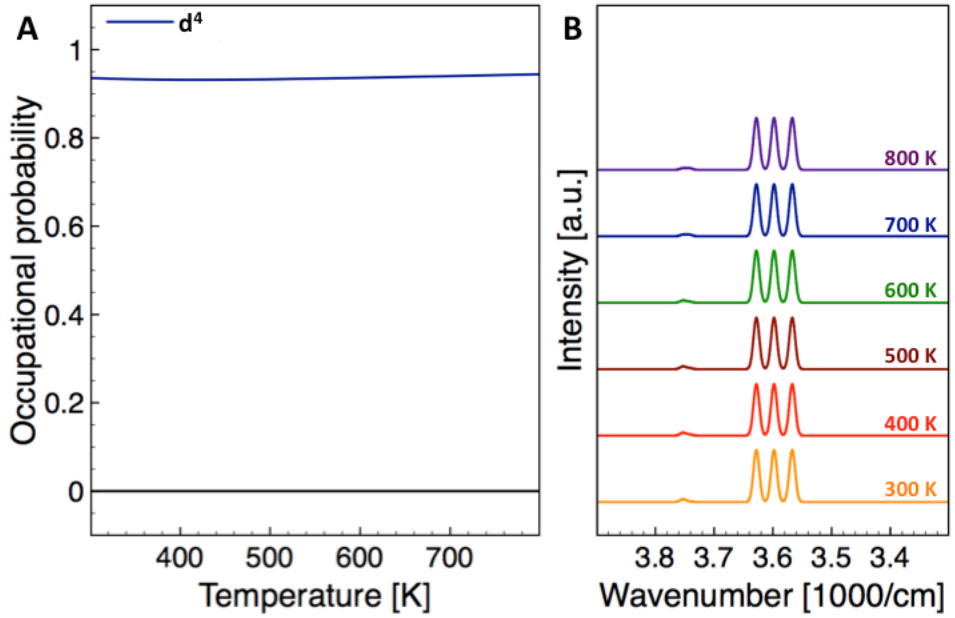

Figure S2: *A: Occupational probabilities for the defect site at a cell volume of 830 Å^3. Occupations below 0.05 were omitted for clarity of the plot. B:Temperature dependent OH vibrational spectrum for the defect sites at a cell volume of 830 Å^3.*

S4: Finite temperature IR spectra of the different Al configurations.

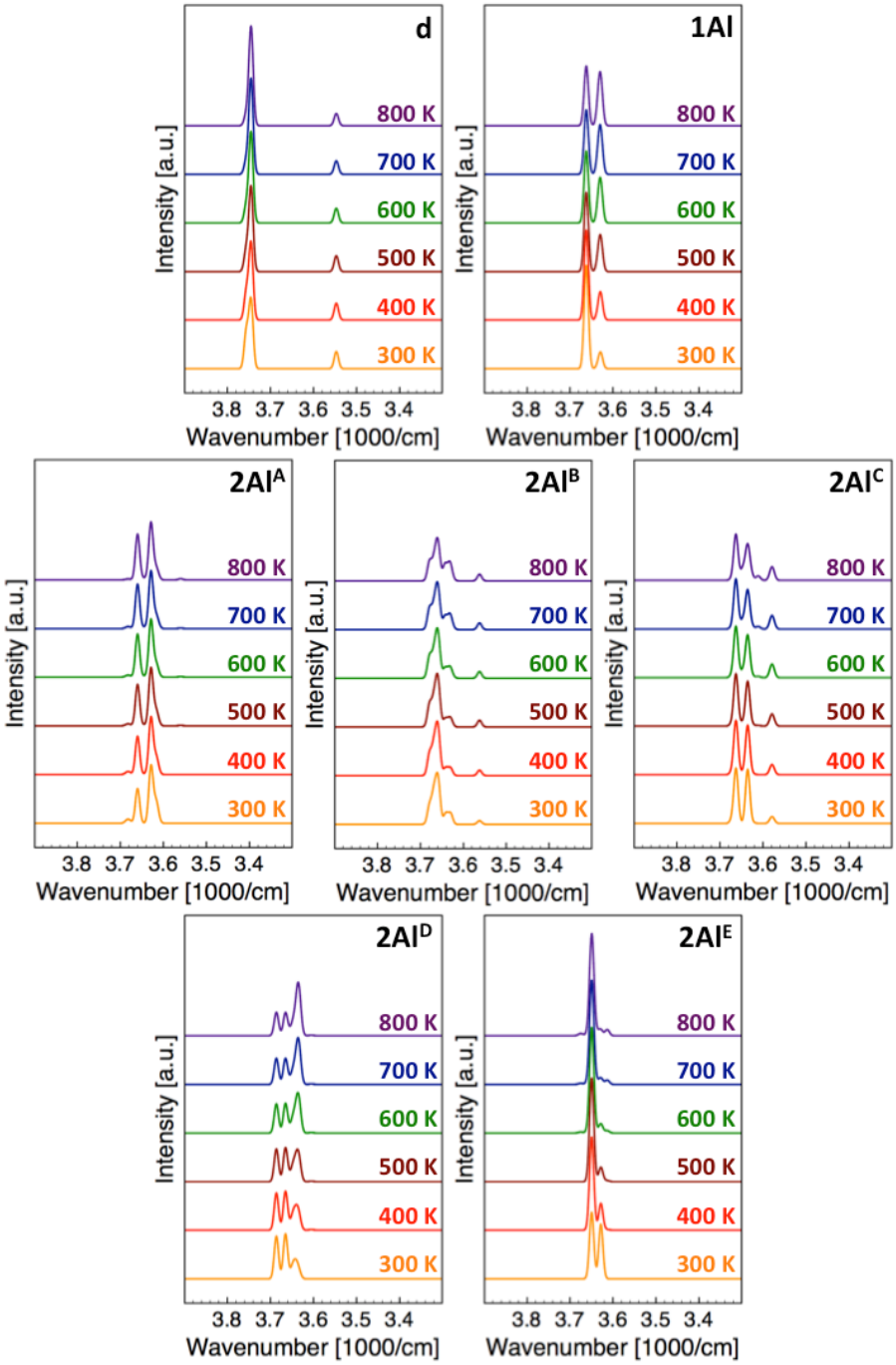

Figure S3: *Temperature dependent OH IR spectra for the different Al distributions and defect site in the zeolite SSZ-13.*

S5: Spectra and intensities for OH-vibrational spectra for the defect site

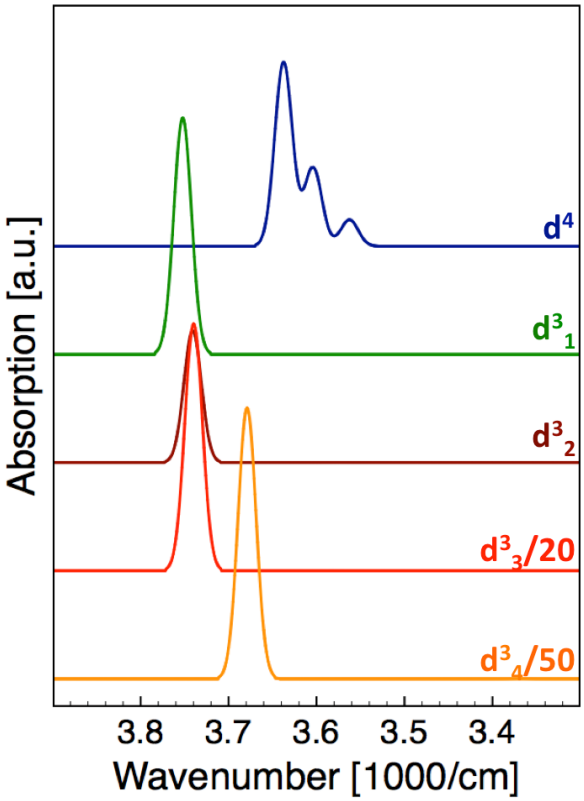

Figure S4: *Spectra for the d site at 810 Å³ calculated using dipole transition moments for intensity. As can be seen in particular for the d³ sites only the highest vibrational frequency contributes. To the observed spectral intensity. Spectra for d³₃ and d³₄ were scaled to arrive at a similar intensity scale. In the calculations of the d site at 830 Å³ similar trends are observed. However, for the d⁴ site three transitions showed similar intensities. We therefore included the three highest wavenumbers in the calculation of the spectrum of d⁴ in Fig. S2 B.*

S6: Temperature dependent ^{27}Al-NMR spectra for the protonated zeolite

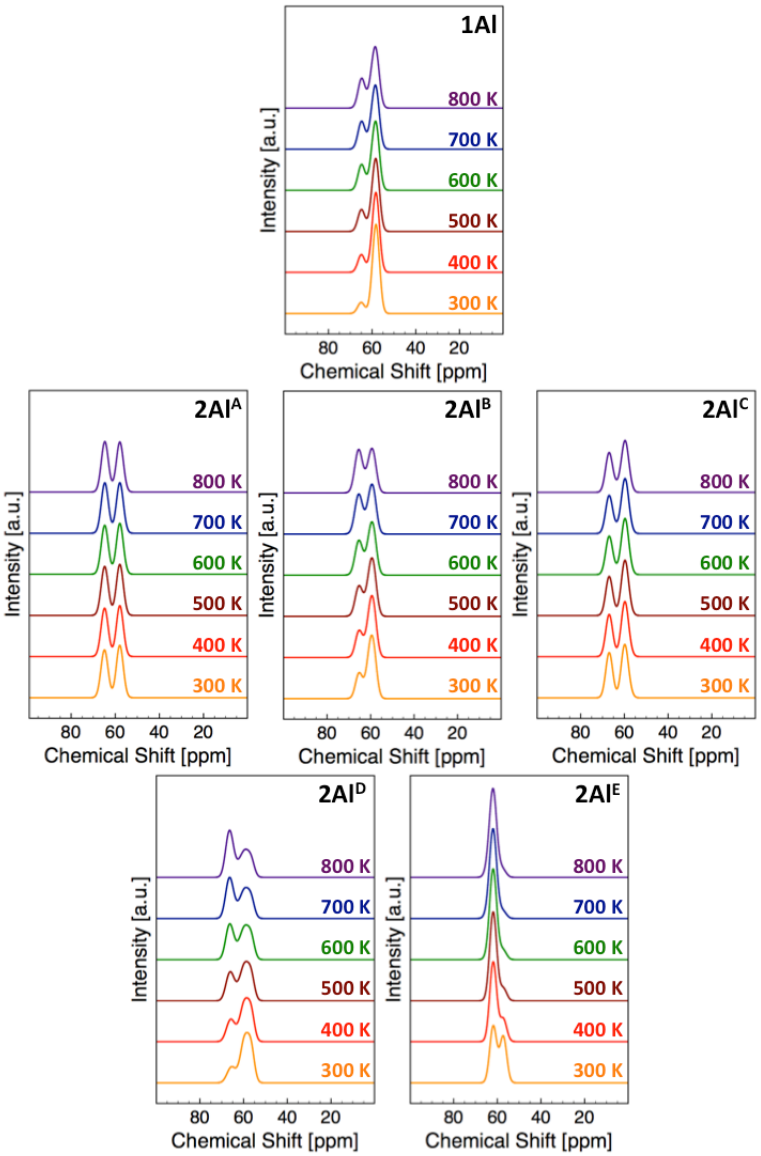

Figure S5: *Temperature dependent ^{27}Al-NMR spectra for the different Al configurations. Each Al configuration leads to a distinct multi-peak spectrum, which is not observed experimentally. Spectra were calculated using Boltzmann probabilities displayed in Fig. 2 of the main text and given in the Supporting Data File.*

S7: ^{29}Si-NMR and ^{27}Al-NMR isotropic chemical shifts for the hydrated sample

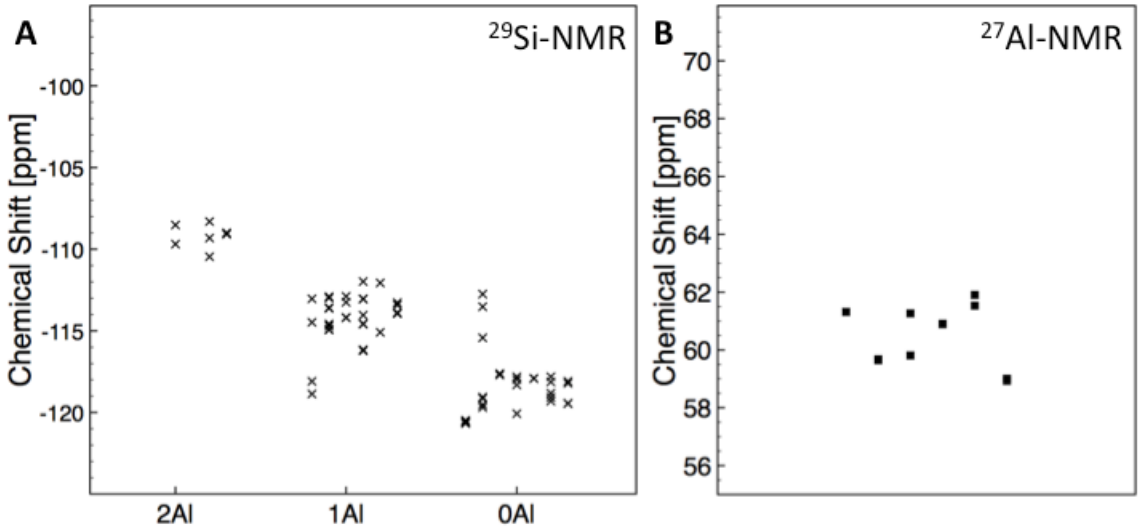

Figure S6: *A: ^{29}Si-NMR isotropic chemical shifts calculated for all modeled SSZ13 structures using a uniform background charge. B: ^{27}Al-NMR isotropic chemical shifts calculated for all modeled SSZ13 structures using a uniform background charge. Columns of data represent (from left to right) 1Al, 2Al^{A}-2Al^{E}. Numerical values for isotropic chemical shifts are given in the Supporting Information.*

S8: ^{27}Al-NMR spectrum

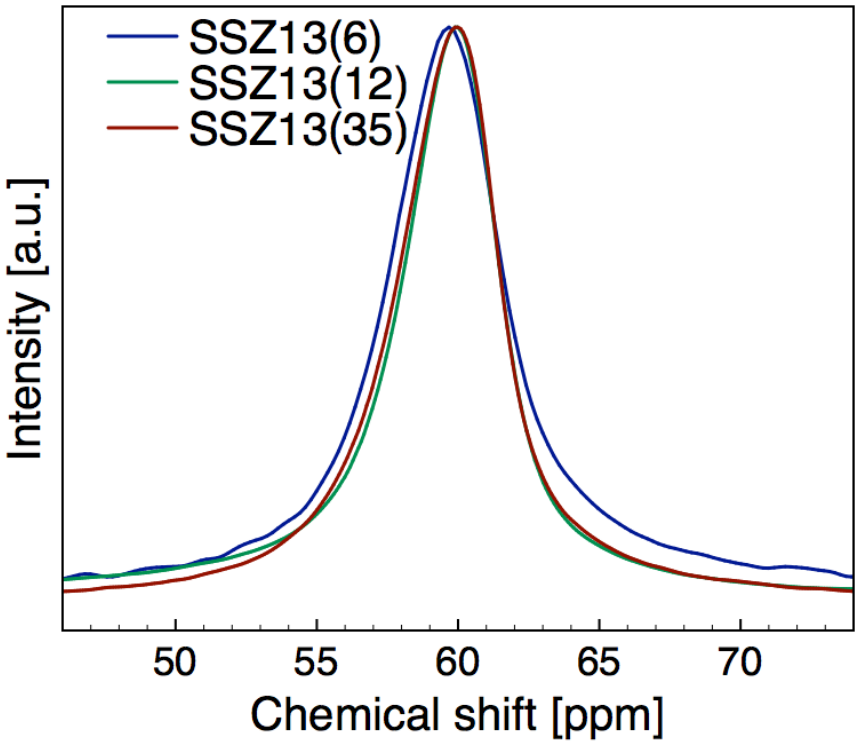

Figure S7: Comparison of ^{27}Al isotropic chemical shifts for SSZ13(6) (blue), SSZ13(12) (green) and SSZ13(35) (red).

S9: Occupational probabilities and temperature dependent OH-IR spectra for the large unit cell

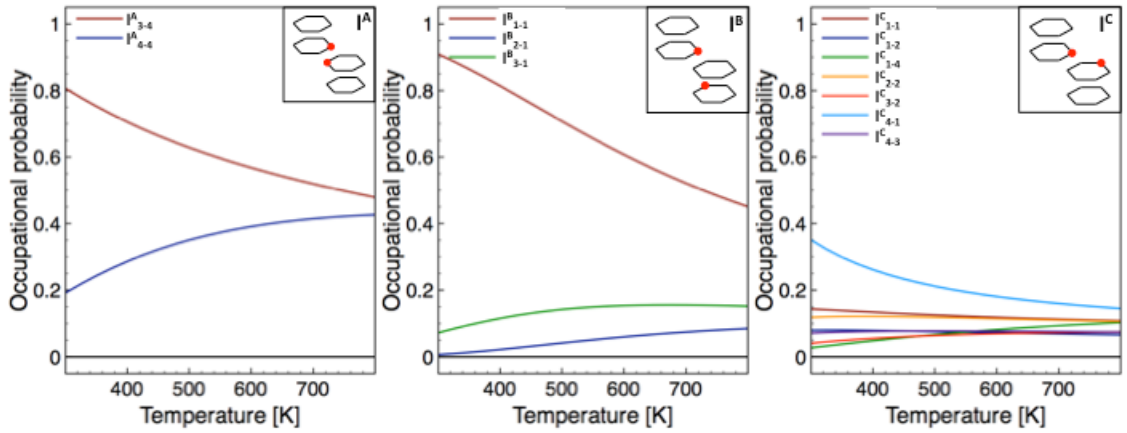

Figure S8: *Occupational probabilities for different proton positions for the local Al and defect distributions shown in Fig 8 of the main text. Occupational probabilities were calculated using Boltzmann weights and the details are given in the main text. Sites with occupations below 0.05 were omitted for clarity.*

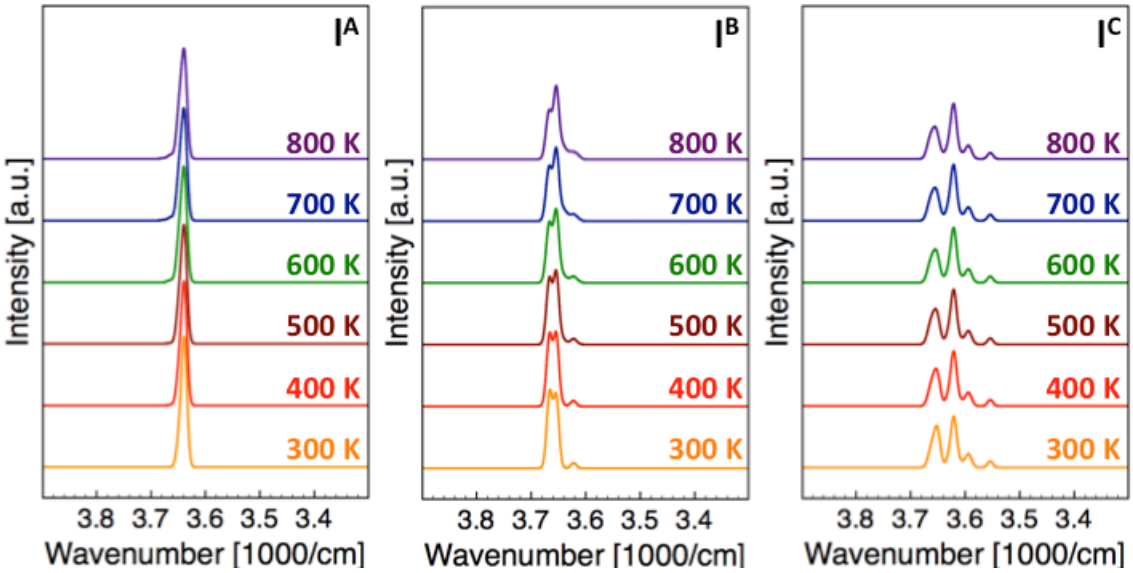

Figure S9: *Temperature dependent OH-IR spectra for the different Al configurations of the large unit cell shown in Fig. 8 of the main text. Each Al configuration leads to a distinct multi-peak spectrum, which is not observed experimentally. Spectra were calculated using Boltzmann probabilities displayed in Fig. S5 and given in the Supporting Data File*

S10: Impact of energy cut-off

In this paper we use an energy cut-off of 420 eV to model the zeolite structures. Here we test the impact of an increase in the energy cut-off to 600 eV for the 1Al configuration. As a first step we test the relative energies calculated at the higher energy cut off (see Tab. S3). As can be seen we find relative energies within 0.001 eV. This indicates that an energy cut-off of 420 eV is an accurate choice for relative energies. In a next step we focus on OH-IR vibrational frequencies. Here we observe a blue shift of ~40 cm^{-1} in all wavenumbers. However, differences in wavenumbers between proton positions are again well reproduced.

Table S3: Relative energies (ΔE), wavenumbers (ν) and relative wavenumbers (Δν) for the 1Al configuration calculated at 420 eV and 600 eV. Relative energies and relative wavenumbers are given with respect to $1Al_1$.

	ΔE [eV]		ν [cm^{-1}]		Δν [cm^{-1}]	
	420 eV	600 eV	420 eV	600 eV	420 eV	600 eV
$1Al_1$	0.000	0.000	3662	3701	0	0
$1Al_2$	0.052	0.053	3628	3669	-35	-32
$1Al_3$	0.085	0.086	3633	3673	-29	-28
$1Al_4$	0.099	0.098	3628	3665	-34	-36

Based on this data we see our choice of an energy cut-off of 420 eV justified. Relative trends are well reproduced and absolute values for wavenumbers agree better with experimental measurements. We attribute this improved agreement with experiments in terms of wavenumber to partial error cancelation in terms of energy cut-off (blue shift) and neglect of anharmonic correction (red shift).